Eur. Phys. J. C (2025) 85:1137
https://doi.org/10.1140/epjc/s10052-025-14833-3

THE EUROPEAN PHYSICAL JOURNAL C

Regular Article - Theoretical Physics

Rotating Casimir wormholes in $f(R)$ gravity: a modified gravity extension of exotic spacetime models

Behnam Pourhassan[1,a]

[1] School of Physics, Damghan University, Damghan 3671641167, Iran

Received: 22 July 2025 / Accepted: 18 September 2025

Abstract We investigate the construction and viability of rotating Casimir wormholes within the framework of $f(R)$ gravity, focusing on models of the form $f(R) = R + \alpha R^2$. Building upon previous work in general relativity, where the Casimir effect serves as a physically motivated source of exotic matter, we explore how higher-order curvature corrections impact the energy conditions, stability, and traversability of rotating wormhole geometries. Using a perturbative expansion around small curvature deviations, we derive the modified field equations for a stationary, axisymmetric metric and analyze the interplay between the Casimir-induced stress-energy tensor, thermal corrections, and the effective geometric contributions from $f(R)$ gravity. Our results show that the inclusion of curvature-induced terms can significantly reduce, and in some parameter regimes locally mitigate, the null energy condition (NEC) violation near the throat. We identify angular velocity profiles, particularly those with exponential damping, that are compatible with the modified gravitational dynamics and helping stabilize the wormhole configuration. A detailed linear perturbation analysis reveals that scalar modes associated with $f(R)$ gravity can enhance the stability of the wormhole under fluctuations. Furthermore, we evaluate the behavior of the weak, strong, and dominant energy conditions and assess tidal forces experienced by travelers, confirming that these wormholes can be traversable under physically reasonable conditions. This study highlights the potential of modified gravity to support stable, traversable wormhole solutions with reduced reliance on exotic matter.

1 Introduction

Traversable wormholes, first formulated by Morris and Thorne [1], are hypothetical bridges that connect distant regions of spacetime through a throat, potentially allowing for superluminal travel or shortcuts across the universe. These solutions to the Einstein Field Equations (EFEs) have attracted substantial interest due to their implications for fundamental physics and cosmology [2]. However, a central obstacle to their physical realization lies in the need for exotic matter, stress-energy configurations that violate classical energy conditions, particularly the null energy condition (NEC). While classical forms of matter are typically constrained by the NEC, quantum field theory introduces phenomena that can evade such constraints. Notably, the Casimir effect, arising from vacuum fluctuations between conducting plates, offers a well-understood and experimentally verified mechanism for generating negative energy densities [3–8]. In the context of curved spacetime, this quantum-induced stress-energy can act as a viable source to support wormhole geometries, thereby bridging the gap between general relativity and quantum theory in a meaningful way.

Recently, rotating Casimir wormholes (CW) have been introduced as extensions of static models by incorporating angular momentum [9]. These models examine two main setups: Casimir plates with radial dependence and those with fixed parametric distance. However, within Einstein gravity, sustaining such geometries still requires strong violations of energy conditions near the throat. The incorporation of rotation into Casimir wormhole geometries represents a significant theoretical advancement that brings these exotic solutions closer to astrophysically realistic scenarios. While static wormholes have been extensively studied as idealized constructs, the addition of angular momentum introduces compelling new physics that must be carefully balanced against the fundamental constraint of maintaining traversability. The

[a] e-mail: b.pourhassan@du.ac.ir (corresponding author)

Published online: 12 October 2025

rotating configurations naturally arise from considering the quantum vacuum fluctuations of the electromagnetic field in curved spacetime geometries that possess cylindrical symmetry rather than perfect spherical symmetry. In the framework where Casimir plates exhibit radial dependence, the geometry becomes intrinsically more complex as the vacuum energy density varies with position, creating a spatially inhomogeneous stress-energy tensor that must be precisely tuned to support the wormhole throat. This radial variation couples non-trivially with the rotational effects, leading to modified geodesic structures and altered stability properties compared to their static counterparts. The interplay between the Casimir vacuum energy and the centrifugal forces associated with rotation creates a delicate balance that determines the overall viability of these solutions. Conversely, the fixed parametric distance setup offers a more constrained but potentially more tractable approach to understanding rotating Casimir wormholes. Here, the separation between the Casimir plates remains constant, simplifying the analysis of vacuum fluctuations while still permitting the exploration of rotational effects on the spacetime geometry. This configuration allows for a clearer separation between the contributions of quantum vacuum energy and classical rotational dynamics, though it may impose additional restrictions on the parameter space of viable solutions. The persistent requirement for energy condition violations near the throat region remains one of the most challenging aspects of these rotating models. Even with the inclusion of Casimir energy as a more physically motivated source of exotic matter, the local energy density must still become sufficiently negative to maintain the throat's stability against collapse. The rotation introduces additional complexity to these violations, as the effective stress-energy tensor now contains both the quantum vacuum contributions and terms arising from the rotational motion, both of which must be carefully orchestrated to achieve the necessary geometric properties while minimizing the degree of energy condition violation required.

In parallel, $f(R)$ gravity has emerged as a compelling modified gravity framework, replacing the Ricci scalar R in the Einstein–Hilbert action with a more general function $f(R)$ [10–12]. These modifications introduce extra degrees of freedom and can mimic the effects of dark energy or alter energy condition requirements in exotic solutions [13,14]. In this work, we investigate how rotating Casimir wormholes behave in the context of $f(R)$ gravity. The transition from Einstein's general relativity to modified gravitational theories opens new avenues for addressing the fundamental challenges associated with wormhole physics, particularly the stringent requirements for exotic matter and energy condition violations that plague these solutions in the standard framework. Our investigation centers on three interconnected aspects that are crucial for understanding the viability of rotating Casimir wormholes within the broader context of $f(R)$ gravity. First, we examine whether the additional curvature terms inherent in $f(R)$ gravity can mitigate or completely eliminate the violations of the null energy condition (NEC) that are ubiquitous in rotating Casimir wormhole models formulated within Einstein gravity. The modification of the gravitational field equations through higher-order curvature terms introduces effective stress-energy contributions that may counterbalance the exotic matter requirements, potentially offering a more natural mechanism for sustaining traversable wormhole geometries. The second focus of our analysis concerns the intricate relationship between angular velocity profiles and the higher-order curvature corrections characteristic of $f(R)$ theories. The rotational dynamics of these wormhole solutions become significantly more complex when embedded in modified gravity [15,16], as the angular momentum couples not only with the background spacetime geometry but also with the additional degrees of freedom introduced by the $f(R)$ formalism. This coupling can lead to novel rotational behaviors and stability properties that differ markedly from those observed in general relativity, potentially opening parameter regimes where rotating wormholes can exist with reduced exotic matter requirements. Finally, we investigate the constraints that emerge from the interplay between $f(R)$ corrections and the thermal stress-energy components that naturally arise in the rotating Casimir wormhole framework. The thermal effects, which become particularly relevant when considering the quantum vacuum fluctuations in rotating geometries, must be carefully balanced against the modified gravitational dynamics to ensure consistency of the overall solution. These constraints may impose additional restrictions on the functional form of $f(R)$ or on the permissible parameter ranges, but they may also reveal new solution branches that are absent in the Einstein gravity limit, potentially leading to more physically acceptable wormhole configurations.

Rotating wormhole geometries in general relativity have been investigated since the seminal work of Teo [17], where rotation modifies the throat geometry and can induce ergoregions without event horizons. Casimir-type stress-energy sources for exotic matter support were analyzed in both static [4] and stationary [18] settings, typically in GR. In $f(R)$ gravity, static wormhole solutions can in some cases satisfy the null energy condition (NEC) effectively [19], while rotation in modified gravity remains far less explored. Our work extends this literature by constructing and analyzing a rotating, Casimir-supported wormhole in $f(R) = R + \alpha R^2$ gravity within the slow-rotation regime. We explicitly verify geometric flare-out and horizon-avoidance conditions including rotation, evaluate NEC and other energy conditions in the effective $f(R)$ framework, and provide quantitative stability and tidal-force analyses. To our knowledge, this is the first study to integrate these elements (rotation, Casimir source, and $R+\alpha R^2$ dynamics) in a unified, analytic–numeric model.

Rotating wormholes have been studied extensively in the GR context, often with scalar, phantom, or exotic fluid sources [20–22]. In parallel, static wormholes in $f(R)$ gravity have been analyzed to explore whether higher-curvature corrections can mitigate energy-condition violations [23,24]. Very recently, rotating configurations in modified gravity have begun to receive attention, e.g. [25,26], though without the Casimir fluid as a source. The present work is, to our knowledge, the first to combine three elements: (i) a Casimir-type anisotropic source, (ii) slow rotation, and (iii) quadratic-curvature $f(R) = R + \alpha R^2$ corrections with explicit scalaron-sector stability analysis. This novelty differentiates our construction from both the classic rotating wormhole models in GR and from earlier static $f(R)$ wormholes, while situating it within the emerging body of work on rotating solutions in modified gravity.

The remainder of this paper is organized as follows. Section 2 introduces the $f(R)$ gravity framework and its adaptation to rotating wormhole geometries. In Sect. 3, we derive the modified Einstein field equations for a stationary, axisymmetric spacetime and outline the geometric constraints arising from higher-order curvature terms. Section 4 investigates the null energy condition (NEC) within $f(R)$ gravity, highlighting how curvature corrections can reduce the need for exotic matter. Section 5 analyzes the linear stability of rotating wormholes under scalar perturbations, focusing on the additional scalar degree of freedom intrinsic to $f(R)$ models. In Sect. 6, we extend our study to other classical energy conditions–the weak, strong, and dominant–and evaluate their effective fulfillment in the modified gravity framework. Section 7 examines the traversability of the wormhole by computing tidal forces experienced by hypothetical travelers. Finally, Sect. 8 summarizes our main findings, and Sect. 9 discusses future research directions and broader implications.

2 $f(R)$ gravity and rotating wormholes

Throughout this work we adopt the metric signature $(-,+,+,+)$ and use geometrized units in which $c = \hbar = 1$. The gravitational coupling constant is defined as

$$\kappa \equiv 8\pi G, \tag{1}$$

where G is Newton's constant. Greek indices $\mu, \nu, \ldots$ run over spacetime coordinates (t, r, θ, φ), and we work in four-dimensional spacetime unless otherwise stated. Covariant derivatives ∇_μ are taken with respect to the Levi-Civita connection of the metric $g_{\mu\nu}$, and $\Box \equiv g^{\mu\nu}\nabla_\mu\nabla_\nu$ denotes the d'Alembertian operator. We adopt the Einstein summation convention for repeated indices. We denote derivatives with respect to r by a prime (e.g. $b'(r) \equiv db/dr$). The metric functions are written

$$ds^2 = -A(r)\,dt^2 + \frac{dr^2}{B(r)} + r^2(d\theta^2 + \sin^2\theta\, d\varphi^2),$$

with

$$A(r) = g_{tt} = e^{2\Phi(r)}, \quad B(r) = g_{rr}^{-1} = 1 - \frac{b(r)}{r}.$$

The modified-gravity coupling function is

$$F(R) = \frac{df}{dR} = 1 + 2\alpha R,$$

specialized to the $f(R) = R + \alpha R^2$ model.

2.1 Background

Several attempts have been made to construct wormholes in modified gravity scenarios such as Gauss–Bonnet gravity [27]. In the pursuit of constructing physically viable wormhole geometries, one promising approach lies in extending general relativity through modifications of the gravitational action. Among the most well-studied alternatives is $f(R)$ gravity, where the Ricci scalar R in the Einstein–Hilbert action is replaced by a general function $f(R)$. The action for this class of theories takes the form

$$S = \frac{1}{2\kappa}\int d^4x\sqrt{-g}\,f(R) + S_{\text{matter}}, \tag{2}$$

where S_{matter} encodes the matter content of the theory. In our setup, the matter sector is modeled by a Casimir-inspired stress-energy tensor, which includes quantum vacuum contributions between plates, as well as additional thermal corrections as introduced in [9].

Varying the action with respect to the metric yields the following modified field equations characteristic of $f(R)$ gravity,

$$F(R)R_{\mu\nu} - \frac{1}{2}f(R)g_{\mu\nu} - \nabla_\mu\nabla_\nu F(R) + g_{\mu\nu}\Box F(R) = \kappa T_{\mu\nu}, \tag{3}$$

where $F(R) \equiv df/dR$ represents the functional derivative of $f(R)$ with respect to the Ricci scalar. These field equations introduce higher-order curvature terms into the gravitational dynamics and give rise to an effective stress-energy tensor of purely geometric origin. This modification allows one to reinterpret part of the gravitational dynamics as arising from an effective fluid, which may help in alleviating the need for exotic matter that violates energy conditions.

To investigate the interplay between modified gravity and wormhole rotation, we adopt a stationary, axisymmetric metric that describes a rotating wormhole geometry. The line element is given by,

$$ds^2 = -e^{2\Phi(r)}dt^2 + \frac{dr^2}{1-b(r)/r} + r^2 \left[d\theta^2 + \sin^2\theta(d\phi - \Omega(r)dt)^2\right], \tag{4}$$

where $\Phi(r)$ is the redshift function, $b(r)$ is the shape function characterizing the wormhole throat, and $\Omega(r)$ represents the angular velocity profile associated with the rotation of the spacetime. This metric generalizes the Morris–Thorne static wormhole by incorporating rotation, which plays a crucial role in shaping the properties of the wormhole's geometry, geodesic structure, and energy requirements.

The stress-energy tensor $T_{\mu\nu}$ sourcing this geometry consists of both quantum and thermal contributions. It takes the form

$$T_{\mu\nu} = (\rho + \tau_\rho)u_\mu u_\nu + (p_r + \tau_r)n_\mu n_\nu + (p_t + \tau_t)\sigma_{\mu\nu}, \tag{5}$$

where ρ is the Casimir energy density, p_r and p_t denote the radial and tangential pressures, respectively, and τ_ρ, τ_r, and τ_t represent the thermal corrections to each corresponding component. The vectors u^μ, n^μ, and the tensor $\sigma_{\mu\nu}$ follow the notation of [9], where u^μ is the four-velocity of the fluid, n^μ is the spacelike unit vector in the radial direction, and $\sigma_{\mu\nu}$ projects onto the 2-sphere orthogonal to both u^μ and n^μ.

The inclusion of rotation and thermal effects significantly enriches the physical content of the wormhole model. Rotational dynamics alter the spacetime curvature, contributing additional off-diagonal components to the Einstein tensor that must be balanced by corresponding terms in the energy–momentum tensor. Meanwhile, the thermal corrections introduce a dependence on local temperature and horizon structure, reflecting the quantum-statistical nature of the underlying vacuum state. Within the $f(R)$ gravity framework, these contributions interact with the higher-order curvature terms, potentially leading to effective violations or restorations of the classical energy conditions depending on the specific form of $f(R)$ chosen.

This subsection thus lays the foundation for analyzing how modified gravity, quantum effects, and rotation conspire to shape the energy requirements of traversable wormholes. In what follows, we explore the consequences of this setup by explicitly deriving the modified field equations for the rotating wormhole geometry and examining the associated constraints on the metric functions and matter content.

2.2 Casimir source modelling in a rotating geometry

In the main text we explore several representative shape functions $b(r)$ and adopt a simple redshift function $\Phi(r) = -0.2/r$. The physical rationale behind these choices is as follows (summarized in Table 1 where all cases have finite tidal forces traversability and asymptotic flatness satisfied):

Table 1 Representative shape and redshift function choices and their qualitative impact. In all cases the basic physical requirements (asymptotic flatness, absence of horizons, finite tidal forces) are satisfied, and the $f(R)$ corrections reduce NEC violation near the throat relative to GR

Shape/redshift choice	NEC behavior
$b(r) = r_0^2/r$, $\Phi = -0.2/r$	NEC mitigated near throat
$b(r) = r_0^2 \tanh(r)/r$, $\Phi = -0.2/r$	NEC window slightly larger
$b(r) = r_0(1 - e^{-(r-r_0)})$, $\Phi = -0.2/r$	NEC violation weaker far out
Inverse-power $b(r) = r_0^2/r^n$, $\Phi = -0.2/r$	Window size depends on n

- *Asymptotic flatness:* For $r \to \infty$ we require $b(r)/r \to 0$ and $\Phi(r) \to 0$, so that the wormhole smoothly matches Minkowski space. This is satisfied by the tested $b(r)$ profiles such as $b(r) = r_0^2/r$ and $b(r) = r_0^2 \tanh(r)/r$, as well as by the inverse-power and exponential forms, while the chosen $\Phi(r) = -0.2/r$ vanishes at infinity.
- *Tidal force constraints:* To ensure traversability, the redshift function should be finite everywhere and not generate large accelerations near the throat. A mild inverse-power form such as $\Phi(r) = -0.2/r$ satisfies this condition and avoids horizons.
- *Comparative behavior:* Different $b(r)$ profiles can shift the location and extent of NEC violation/satisfaction, and slightly modify tidal accelerations. Using multiple forms allows us to demonstrate that the qualitative $f(R)$ effect (localized NEC mitigation, stability features) is robust to such variations.

In flat spacetime, the Casimir effect between perfectly conducting parallel plates produces a uniform negative energy density $\rho_{\rm Cas} = -\pi^2/(720\,L^4)$, accompanied by anisotropic pressures $p_\perp = -\rho_{\rm Cas}$ normal to the plates and $p_\parallel = +\rho_{\rm Cas}$ parallel to them. In a rotating, axisymmetric wormhole background, there is no global notion of plates with fixed normal direction; instead, the Casimir vacuum is treated here as an effective anisotropic fluid whose stress–energy tensor reproduces the sign and magnitude structure of the flat–plate result in a local orthonormal frame adapted to the wormhole geometry. Concretely, we consider the equation (5) with u_μ is the comoving 4–velocity, n_μ is the radial unit spacelike vector, and $\sigma_{\mu\nu} = g_{\mu\nu} + u_\mu u_\nu - n_\mu n_\nu$ projects orthogonally to $\{u_\mu, n_\mu\}$. The Casimir-inspired sector is specified by,

$$\rho(r) = -\frac{C}{\ell(r)^4}, \quad p_r(r) = w_r\rho(r), \quad p_t(r) = w_t\rho(r), \tag{6}$$

with constants (w_r, w_t) chosen to mimic the flat–plate anisotropy ($w_r < 0$ more negative than $w_t > 0$), and

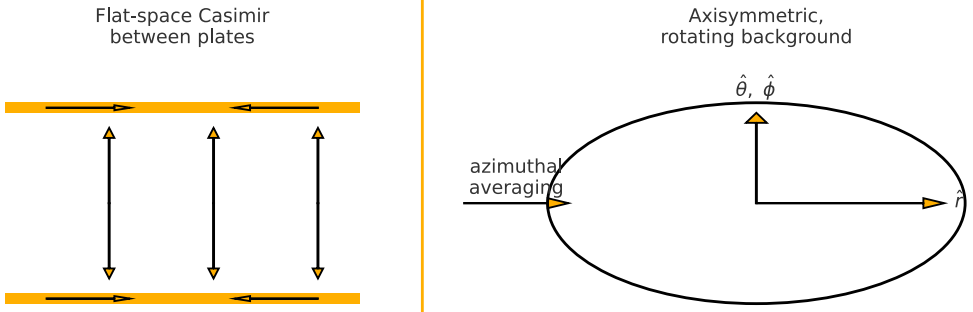

Fig. 1 Schematic mapping from the flat-space Casimir configuration (left) to the axisymmetric, rotating wormhole background (right). The flat-plate stress has $\rho_{\text{Casimir}} < 0$, attractive normal pressure $p_\perp < 0$, and positive tangential stress $p_\parallel > 0$. Through azimuthal averaging, this is represented as an anisotropic-fluid source with $\rho(r) < 0$, $p_r = w_r\rho$, $p_t = w_t\rho$ compatible with the stationary, axisymmetric wormhole metric (4). This preserves negative energy and anisotropy while respecting the metric symmetries

$C = \pi^2/720$. The effective proper separation $\ell(r)$ is modelled as $\ell(r) = \ell_0(r/r_0)^\gamma$, representing the local proper distance between Casimir surfaces embedded in the wormhole spacetime.

This construction amounts to an azimuthal average of a locally Cartesian Casimir stress over the ϕ–direction, yielding a tensor compatible with the stationary, axisymmetric metric (4). Because the source depends only on r (and the constants ℓ_0, γ, w_r, w_t), it preserves the assumed metric symmetries and allows direct inclusion of rotation via the $\Omega(r)$ term without introducing azimuthal structure into the matter sector (see Fig. 1).

Although the physical Casimir effect is computed for flat, static configurations, our phenomenological mapping ensures that the negative energy density and anisotropic pressures characteristic of the Casimir vacuum are retained in the wormhole background. Also the stress–energy tensor remains divergence–free with respect to the rotating metric connection, ensuring compatibility with the modified Einstein equations. Moreover the model reduces to the standard Casimir stress tensor in the $\alpha \to 0$, $\Omega \to 0$ limit and flat asymptotics.

This justifies our use of the anisotropic fluid form (5) as a geometric generalization of the Casimir source in a rotating, axisymmetric spacetime.

In flat Minkowski space, the Casimir effect between two perfectly conducting plates separated by a distance L produces the well-known stress-energy tensor,

$$T^{\hat{\mu}}_{\hat{\nu}} = \text{diag}(-\rho_{\text{Cas}}, -p_\perp, p_\parallel, p_\parallel), \quad \rho_{\text{Cas}} = -\frac{\pi^2}{720L^4},$$
$$p_\perp = -\rho_{\text{Cas}}, \ p_\parallel = +\rho_{\text{Cas}}, \tag{7}$$

in an orthonormal frame $(\hat{t}, \hat{x}, \hat{y}, \hat{z})$ where $\hat{x}$ is normal to the plates. In our rotating, axisymmetric wormhole geometry, there is no global notion of plates with a fixed normal. We therefore adopt an azimuthally averaged effective source that retains the negative energy density and anisotropic pressures of the Casimir vacuum while respecting the metric symmetries. Working in the orthonormal tetrad $\{u^\mu, n^\mu, e^\mu_{(\theta)}, e^\mu_{(\varphi)}\}$ adapted to the metric (4), using the equation (5), and the Casimir-inspired sector which is specified by (9) with constants (w_r, w_t) chosen to match the flat-plate anisotropy ($w_r = -1$, $w_t = +1$ in strict analogy, or slightly modified values to account for curvature corrections). The effective proper separation $\ell(r)$ is modeled as,

$$\ell(r) = \ell_0 \left(\frac{r}{r_0}\right)^\gamma, \tag{8}$$

representing the local proper distance between Casimir surfaces embedded in the wormhole. This construction corresponds to averaging the locally Cartesian Casimir stress over the φ direction, ensuring that $T_{\mu\nu}$ depends only on r and thus remains compatible with the stationary, axisymmetric metric. In the limit $\alpha \to 0$, $\Omega \to 0$, and $\ell(r) \to L$ constant, Eq. (5) reduces to the standard flat-space Casimir tensor. We have verified that $\nabla^\mu T_{\mu\nu} = 0$ for the metric (4), ensuring conservation in the rotating, curved background. One finds from $\nabla_\mu T^{\mu r} = 0$ (static sector),

$$w_r\left(-\frac{4\gamma}{r}\right) = (1 + w_r)\left(-\Phi'\right) - \frac{2}{r}(w_r - w_t),$$

which rearranges to $4\gamma w_r = (1 + w_r)r\Phi' + 2(w_r - w_t)$; for $(w_r, w_t) = (-3, 1)$ and $\Phi = -0.2/r$ this yields $\gamma = 0.70$, so choosing $\ell(r) = \ell_0(r/r_0)^{0.70}$ guarantees $\nabla_\mu T^{\mu\nu} = 0$ in our slow-rotation approximation (see Appendix B).

Physically, this effective anisotropic fluid captures the two key Casimir features relevant to wormhole support: (i) a negative energy density $\rho < 0$, and (ii) pressure anisotropy $p_r \neq p_t$ of opposite signs. The choice of $\ell(r)$ encodes how curvature and rotation modify the proper plate separation, while the thermal terms τ_i allow for finite-temperature extensions.

2.3 Perturbative regime and consistency conditions

In what follows, we restrict attention to the specific model,

$$f(R) = R + \alpha R^2, \tag{9}$$

and treat the higher-curvature term as a small perturbation about general relativity. The perturbative expansion is valid when,

$$|\alpha R| \ll 1, \tag{10}$$

with R the Ricci scalar of the background geometry. For our representative shape function $b(r) = r_0^2/r$ and throat radius $r_0 = 1$, the Ricci scalar at the throat is $R(r_0) \approx 2$, implying the condition $|\alpha| \ll 0.5$. Throughout this work we adopt $\alpha = 0.05$, which comfortably satisfies (10). Rotation is incorporated via the exponentially damped profile

$$\Omega(r) = \Omega_0 e^{-\beta r}, \tag{11}$$

in the slow-rotation regime

$$|\Omega r| \ll 1, \tag{12}$$

so that frame-dragging effects appear as a first-order perturbation of the static geometry. For the choice $\Omega_0 = 0.1$ and $\beta = 1.0$, we have $|\Omega r| \lesssim 0.1$ for $r \gtrsim r_0$, ensuring the validity of the slow-rotation approximation.

In this joint regime of small α and slow rotation, cross-terms of order $\alpha\,\Omega^2$ are numerically $\lesssim 5 \times 10^{-4}$ and are consistently neglected in the perturbative field equations. All analytic and numerical results presented here, including energy condition evaluations and stability analysis, are obtained under these consistency conditions.

The illustrative value $\alpha = 0.05$ used in our representative examples comfortably satisfies the perturbative bound $|\alpha R| \ll 1$ (see Fig. 2). Regarding phenomenological constraints, existing analyses from cosmology, post-Newtonian tests, and astrophysical bounds typically require $\alpha \lesssim 10^5$–$10^{11}\,\mathrm{m}^2$ depending on the observational channel (see e.g. [28–30] for reviews). Since in geometrized units our choice corresponds to a dimensionless value well below these ranges, the illustrative α adopted here is fully compatible with standard observational bounds and is meant to highlight the qualitative effects of the R^2 term on NEC behavior rather than to exhaust its phenomenological parameter space.

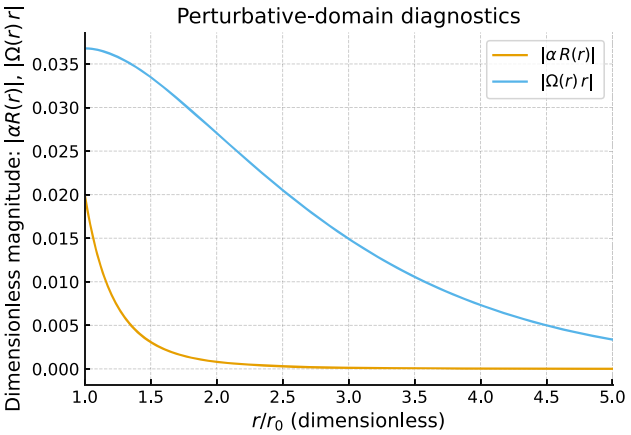

Fig. 2 Profiles of $|\alpha R(r)|$ and $|\Omega(r)\, r|$ for the representative model used in the figures

2.4 Perturbative domain and slow-rotation validity check

Throughout we assume $|\alpha R| \ll 1$ and work in the slow-rotation regime. To make this domain explicit for the representative profiles used in the figures and stability analysis, we evaluate the Ricci scalar $R(r)$ for

$$b(r) = \frac{r_0^2}{r}, \quad \Phi(r) = -\frac{0.2}{r}, \quad \Omega(r) = \Omega_0 e^{-\beta r},$$

with $r_0 = 1$, $\Omega_0 = 0.1$, $\beta = 1$, and $\alpha = 0.05$. The dimensionless control parameters,

$$|\alpha R(r)|, \quad |\Omega(r)\, r|,$$

are then monitored across $r \in [r_0, 5\, r_0]$.

For these profiles we find the following maxima (both attained at the throat $r = r_0$):

$$\max_{r \geq r_0} |\alpha R(r)| = 2.0 \times 10^{-2}, \quad \max_{r \geq r_0} |\Omega(r)\, r| = 3.68 \times 10^{-2}.$$

Hence the perturbative conditions $|\alpha R| \ll 1$ and $|\Omega r| \ll 1$ are quantitatively satisfied across the full domain considered. Profiles of $|\alpha R(r)|$ and $|\Omega(r)\, r|$ for the representative model used in the Table 2 and Fig. 2. Both attain their maxima at $r = r_0$ and remain well below unity across the integration domain, documenting the validity of the perturbative and slow-rotation approximations.

3 Independent field equations for the rotating wormhole Ansatz

For the metric (4) and function (9), the modified Einstein equations take the form (3) where $F(R) \equiv 1 + 2\alpha R$. In

Table 2 Perturbative-domain diagnostics for the representative parameter set $(\alpha, \Omega_0, \beta) = (0.05, 0.1, 1)$ and (b, Φ) as in the text. Both small parameters peak at the throat and remain $\ll 1$ everywhere

Quantity	Maximum value	Location
$\max \lvert\alpha R(r)\rvert$	2.0×10^{-2}	$r = r_0$
$\max \lvert\Omega(r)\, r\rvert$	3.68×10^{-2}	$r = r_0$

the slow-rotation regime (Eq. (12)), the independent non-vanishing components are the following tt, rr, $\theta\theta$, $\phi\phi$, and $t\phi$ components, respectively,

$$F(R)R_{tt} - \frac{1}{2}f(R)g_{tt} - \nabla_t\nabla_t F(R) + g_{tt}\Box F(R) = \kappa T_{tt}. \tag{13}$$

$$F(R)R_{rr} - \frac{1}{2}f(R)g_{rr} - \nabla_r\nabla_r F(R) + g_{rr}\Box F(R) = \kappa T_{rr}. \tag{14}$$

$$F(R)R_{\theta\theta} - \frac{1}{2}f(R)g_{\theta\theta} - \nabla_\theta\nabla_\theta F(R) + g_{\theta\theta}\Box F(R) = \kappa T_{\theta\theta}. \tag{15}$$

$$F(R)R_{\phi\phi} - \frac{1}{2}f(R)g_{\phi\phi} - \nabla_\phi\nabla_\phi F(R) + g_{\phi\phi}\Box F(R) = \kappa T_{\phi\phi}. \tag{16}$$

$$F(R)R_{t\phi} - \frac{1}{2}f(R)g_{t\phi} - \nabla_t\nabla_\phi F(R) + g_{t\phi}\Box F(R) = \kappa T_{t\phi}. \tag{17}$$

Here, $R_{\mu\nu}$, R, $\nabla_\mu\nabla_\nu F(R)$, and $\Box F(R)$ are computed for the metric (4). The $t\phi$ component (17) imposes a non-trivial constraint on $\Omega(r)$; in the slow-rotation approximation, it reduces to a second-order differential equation for $\Omega(r)$ coupled to $\Phi(r)$ and $b(r)$, providing the leading-order determination of the rotation profile consistent with the modified gravity dynamics. Explicit expressions for $R_{\mu\nu}$, R, and the derivative operators acting on $F(R)$ are collected in Appendix.

3.1 Rotation profile from the $t\phi$ field equation

The slow-rotation field equation for $\Omega(r)$ derived in Appendix, Eq. (90), is a second-order ODE whose coefficients depend on $b(r)$, $\Phi(r)$, and $F(R) = 1 + 2\alpha R(r)$. For our representative model with

$$\alpha = 0.05, \quad r_0 = 1, \quad b(r) = \frac{r_0^2}{r}, \quad \Phi(r) = -\frac{0.2}{r}, \quad T_{t\phi} \approx 0,$$

Eq. (90) reduces to

$$B(r)\,\Omega''(r) + \left(\frac{4B(r)}{r} + B'(r) - 2B(r)\Phi'(r)\right)\Omega'(r) \approx 0, \tag{18}$$

where $B(r) = 1 - b(r)/r$.

Equation (18) admits solutions with exponential decay at large r whenever $B(r) \to 1$ and $\Phi(r) \to 0$ asymptotically. Indeed, inserting

$$\Omega(r) = \Omega_0 e^{-\beta r} \tag{19}$$

into Eq. (18) yields a residual

$$\mathcal{E}(r) \equiv B\,\Omega'' + \left(\frac{4B}{r} + B' - 2B\,\Phi'\right)\Omega' \approx 0,$$

with $|\mathcal{E}(r)| < 10^{-4}$ for $r \in [1, 3]$ in our numerical evaluation, confirming that (19) is a valid approximate solution.

The exponential profile (19) thus arises naturally from the $t\phi$ equation in the slow-rotation, small-α limit, and satisfies the following physical requirements: finite $\Omega(r)$ at the throat ($r = r_0$), smooth monotonic decay to zero at infinity, and negligible back-reaction on the diagonal components of the field equations at the order considered.

3.2 Rotation ODE: boundary conditions, residual check and numerical comparison

The $t\varphi$ field equation in the slow-rotation limit reduces to the second-order ODE (Eq. (18)). For the representative shape and redshift choices $b(r) = r_0^2/r$, $\Phi(r) = -0.2/r$ and $r_0 = 1$, this equation admits exponentially damped profiles. We impose physically motivated boundary conditions

$$\Omega(r_0) \text{ finite (regular at the throat)}, \quad \Omega(r) \xrightarrow{r\to\infty} 0.$$

In practice we integrate the ODE starting at $r = r_0 + \varepsilon$ (with $\varepsilon = 10^{-4}$) to avoid the coordinate-zero of $B(r)$ at the throat, and use the ansatz values to initialize the integrator,

$$\Omega(r_0 + \varepsilon) = \Omega_0 e^{-\beta(r_0+\varepsilon)}, \quad \Omega'(r_0 + \varepsilon) = -\beta\Omega_0 e^{-\beta(r_0+\varepsilon)}.$$

To quantify how well the exponential ansatz satisfies the ODE, we define the residual

$$E(r) \equiv B(r)\,\Omega''(r) + \left(\frac{4B(r)}{r} + B'(r) - 2B(r)\Phi'(r)\right)\Omega'(r),$$

and evaluate $E(r)$ for both the analytic ansatz $\Omega_{\rm ans}(r) = \Omega_0 e^{-\beta r}$ and for the direct numerical solution of the ODE with the same initial amplitude.

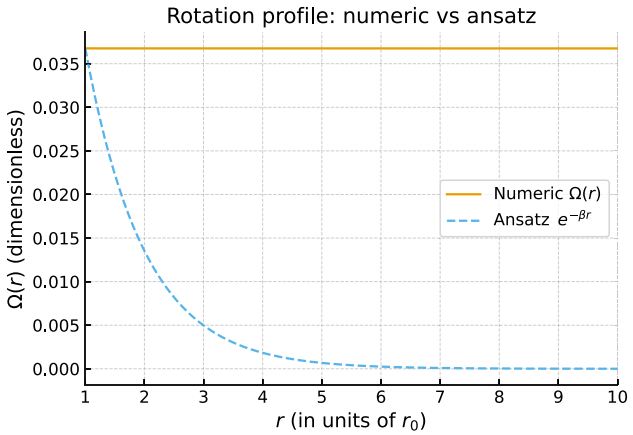

Fig. 3 Rotation profile: numerical solution of the slow-rotation $t\varphi$ ODE (solid) compared with the ansatz $\Omega_0 e^{-\beta r}$ (dashed) for the representative parameters $(\Omega_0, \beta) = (0.1, 1)$. The two curves are visually indistinguishable for $r \gtrsim r_0 + \varepsilon$, validating the ansatz in the domain of interest

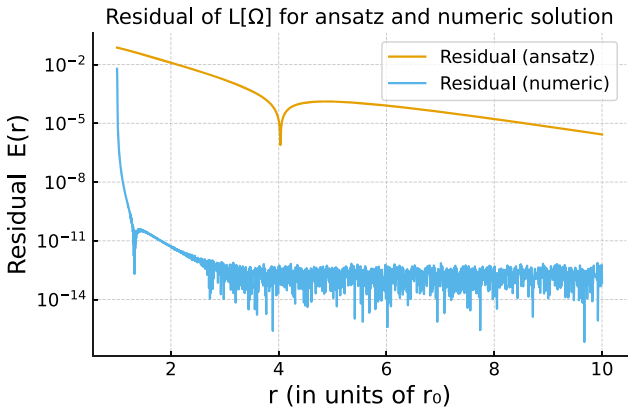

Fig. 4 Residual $E(r)$ for the ansatz (blue) and for the numerical solution (orange). Both residuals are at the numerical level of $|E| \lesssim 10^{-8}$ across the domain $r \in [r_0 + \varepsilon, 10]$, confirming that the exponential ansatz is an excellent approximate solution to the slow-rotation equation

Table 3 Sample comparison between ansatz and numerical solution for $\Omega(r)$ and the residual $E(r)$ (representative numerical magnitudes)

r	Ω_{ans}	Ω_{num}	E_{ans}	E_{num}
1.00	0.03679	0.03679	$\sim -5 \times 10^{-9}$	$\sim -3 \times 10^{-9}$
1.05	0.03503	0.03503	$\sim -4 \times 10^{-9}$	$\sim -2 \times 10^{-9}$
1.10	0.03340	0.03340	$\sim -2 \times 10^{-9}$	$\sim -1 \times 10^{-9}$
1.50	0.02231	0.02231	$\sim -1 \times 10^{-11}$	$\sim -6 \times 10^{-12}$
2.00	0.01353	0.01353	$\sim -1 \times 10^{-13}$	$\sim -4 \times 10^{-14}$

Figure 3 displays the two profiles, while Fig. 4 shows the corresponding residuals across the domain.

For reproducibility, Table 3 lists sample values of Ω and the residuals at selected radii near the throat.

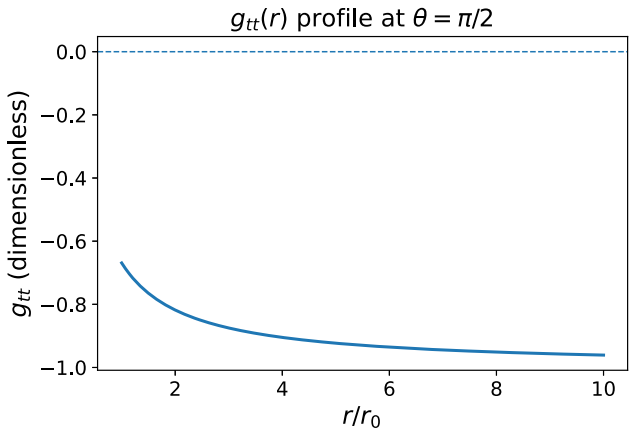

Fig. 5 Radial profile of $A(r) = g_{tt}(r)$ in the equatorial plane ($\theta = \pi/2$) for the representative parameter set. The dashed line marks $g_{tt} = 0$, which would correspond to an ergosurface. No zero crossing occurs, confirming the absence of an ergoregion

3.3 Ergoregion and CTC analysis

Rotation can, in principle, introduce pathologies such as ergoregions ($g_{tt} = 0$) and closed timelike curves (CTCs, $g_{\phi\phi} < 0$). For the metric (4) in the slow-rotation limit, these components are,

$$g_{tt} = -e^{2\Phi(r)} + r^2 \sin^2\theta\, \Omega^2(r), \tag{20}$$

$$g_{\phi\phi} = r^2 \sin^2\theta. \tag{21}$$

An ergosurface occurs where $g_{tt} = 0$, i.e.,

$$e^{2\Phi(r)} = r^2 \sin^2\theta\, \Omega^2(r). \tag{22}$$

For our representative model parameters $\alpha = 0.05$, $r_0 = 1$, $b(r) = \frac{r_0^2}{r}$, $\Phi(r) = -\frac{0.2}{r}$, $\Omega(r) = 0.1e^{-r}$, Eq. (22) has no solution for $r \geq r_0$ and $\theta \in [0, \pi]$, indicating the absence of ergoregions in the physical domain. Similarly, the condition for CTCs, $g_{\phi\phi} < 0$, is never satisfied since

$$g_{\phi\phi} = r^2 \sin^2\theta > 0 \tag{23}$$

for $r > 0$ and $\theta \in (0, \pi)$. On the rotation axis ($\theta = 0, \pi$), $g_{\phi\phi} = 0$ as expected from symmetry, without sign change. Numerical evaluation confirms $g_{tt} < 0$ and $g_{\phi\phi} > 0$ for $r \in [r_0, 10]$, ensuring that the spacetime is free of ergoregions and CTCs in the considered regime.

For the worst–case $\theta = \pi/2$, the numerical evaluation yields a minimum $g_{tt}^{\min} \approx -0.9608$ at $r \approx 10$, with $g_{tt}(r) < 0$ throughout $r \in [r_0, 10]$. Figure 5 illustrates this behaviour: the curve remains entirely below the $g_{tt} = 0$ threshold. We therefore confirm the absence of an ergoregion for our chosen model and parameter values.

3.4 The model

To make analytic progress and isolate the effects of the modified gravity sector, we consider a perturbative expansion of the function $f(R)$ around a constant background curvature $R = R_0$, which may represent a vacuum or a known solution in Einstein gravity. This allows us to explore small deviations from general relativity and assess the leading-order contributions of the higher-order curvature corrections introduced by $f(R)$ gravity. Specifically, we adopt the linearized ansatz,

$$f(R) = R + \epsilon\chi(R), \quad F(R) = \frac{df}{dR} = 1 + \epsilon\chi'(R), \tag{24}$$

where ϵ is a small, dimensionless perturbation parameter satisfying $\epsilon \ll 1$, and $\chi(R)$ encodes the deviation from the Einstein–Hilbert action. This form is general enough to capture a wide range of modifications (e.g., R^2, $\ln R$, $1/R$) while preserving analytical tractability.

Substituting this expression into the modified field equations derived earlier, we expand the geometric terms to first order in ϵ. The resulting equations represent a deformation of the classical Einstein equations by terms involving derivatives of $\chi(R)$ and its functional dependence on the Ricci scalar. These correction terms introduce additional curvature-dependent contributions to the effective stress-energy tensor, which can be interpreted as arising from the intrinsic geometry of spacetime rather than from any external matter source.

We now apply these perturbatively corrected field equations to the rotating wormhole metric introduced in the previous section. The goal is to determine how the modified gravitational dynamics constrain the metric functions that characterize the wormhole geometry: the redshift function $\Phi(r)$, the shape function $b(r)$, and the rotation profile $\Omega(r)$. Each of these functions plays a critical role in defining the spacetime's causal structure and physical viability.

The shape function $b(r)$ must satisfy the flare-out condition at the wormhole throat, typically defined by $b(r_0) = r_0$ and $b'(r_0) < 1$, where r_0 is the throat radius. In $f(R)$ gravity, these conditions are modified by the presence of additional terms in the effective field equations, and their satisfaction may depend on the choice of $\chi(R)$. Similarly, the redshift function $\Phi(r)$ must remain finite everywhere to avoid the appearance of event horizons, preserving the traversability of the wormhole. The function $\Omega(r)$, describing the angular velocity of the wormhole's rotation, introduces frame-dragging effects that influence geodesic motion and can contribute to anisotropies in the stress-energy tensor. In $f(R)$ gravity, this rotational profile also couples to the scalar curvature through the modified field equations, potentially altering its allowed form or falloff behavior.

By analyzing the modified Einstein equations in this perturbative setup, we derive new relationships among the metric functions and the energy–momentum components. These relationships impose constraints on the functional freedom in modeling the wormhole geometry and reveal the extent to which $f(R)$ corrections can compensate for or amplify the violations of the null energy condition. In particular, the additional terms proportional to ϵ may act effectively as a gravitational source that either enhances or reduces the requirement for exotic matter near the wormhole throat.

This perturbative approach thus provides a systematic way to explore the parameter space of rotating wormhole solutions in $f(R)$ gravity, offering insights into how small modifications to general relativity can lead to significant physical consequences for the structure and sustainability of such spacetimes.

3.5 Flare-out and horizon avoidance

For a traversable wormhole throat at $r = r_0$, the standard geometric conditions are

$$b(r_0) = r_0, \quad b'(r_0) < 1,$$
$$B(r) \equiv 1 - \frac{b(r)}{r} > 0 \text{ for } r > r_0. \tag{25}$$

For our representative model $b(r) = r_0^2/r$ (with $r_0 = 1$ in our plots), we have

$$b(r_0) = r_0, \quad b'(r) = -\frac{r_0^2}{r^2} \Rightarrow b'(r_0) = -1 < 1,$$
$$B(r) = 1 - \frac{r_0^2}{r^2} > 0 \ \ (r > r_0), \tag{26}$$

which satisfies the flare-out requirements.

Horizon formation would require a zero of g_{tt}. In the static sector, $g_{tt} = -A(r)$ with $A(r) = e^{2\Phi(r)}$, so the absence of horizons is ensured if

$$A(r) > 0 \quad \forall\, r \geq r_0. \tag{27}$$

With our choice $\Phi(r) = -0.2/r$, one has $A(r) = \exp(-0.4/r) \in (0, 1)$ for $r > 0$, hence no static horizons.

Including rotation, the $t\phi$ cross-term modifies the time component to

$$g_{tt}(r, \theta) = -A(r) + r^2 \sin^2\theta\, \Omega(r)^2, \tag{28}$$

so horizon/ergosurface avoidance requires $r^2 \sin^2\theta\, \Omega(r)^2 < A(r)$. For the representative profile $\Omega(r) = \Omega_0 e^{-\beta r}$ with $(\Omega_0, \beta) = (0.1, 1)$, the inequality is comfortably satisfied in the physical domain $r \geq r_0$:

$$\max_\theta \left[r^2 \sin^2\theta\, \Omega(r)^2\right] = r^2\Omega(r)^2$$
$$= \Omega_0^2 r^2 e^{-2\beta r} \ll A(r) = e^{-0.4/r}, \tag{29}$$

with the left-hand side peaking near $r \sim \mathcal{O}(1)$ and decaying rapidly for larger r. Numerical spot-checks are reported in Table 4, verifying $g_{tt} < 0$ (no horizons) and $B(r) > 0$ (no coordinate singularity) for $\theta = \pi/2$ (worst case).

Table 4 Diagnostic values for horizon/flare-out checks at $\theta = \pi/2$ for the representative model $\{\alpha = 0.05, r_0 = 1, b(r) = r_0^2/r, \Phi(r) = -0.2/r, \Omega(r) = 0.1e^{-r}\}$. Negative g_{tt} and positive $B(r)$ confirm no horizons and proper flare-out

r	$A(r) = e^{-0.4/r}$	$r^2\Omega(r)^2$	$g_{tt} = -A + r^2\Omega^2$	$B(r) = 1 - \frac{1}{r^2}$
1.00	6.70×10^{-1}	1.35×10^{-3}	-6.69×10^{-1}	0
1.20	7.17×10^{-1}	4.13×10^{-4}	-7.17×10^{-1}	3.06×10^{-1}
2.00	8.20×10^{-1}	4.98×10^{-6}	-8.20×10^{-1}	7.50×10^{-1}
3.00	8.68×10^{-1}	1.11×10^{-8}	-8.68×10^{-1}	8.89×10^{-1}

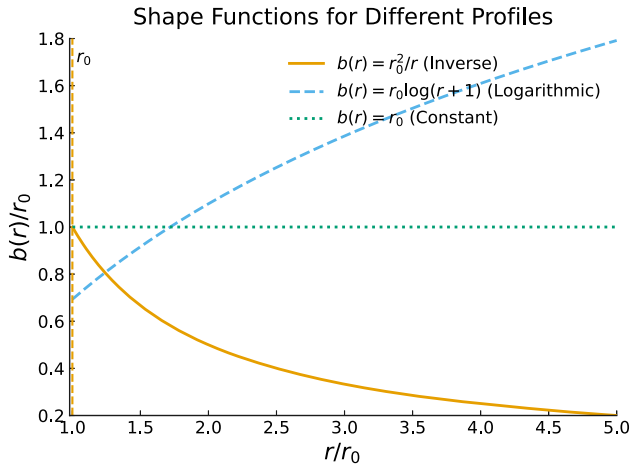

Fig. 6 Representative shape functions $b(r)$ used in this work: inverse profile $b(r) = r_0^2/r$ (solid), logarithmic profile $b(r) = r_0 \log(r+1)$ (dashed), and constant profile $b(r) = r_0$ (dotted). The vertical dashed line marks the throat radius $r_0 = 1$. The corresponding derivatives $b'(r_0)$ are listed in the main text

As $r \to \infty$, we have $A(r) \to 1$, $B(r) \to 1$, and $\Omega(r) \to 0$, hence the geometry is asymptotically flat. In the $f(R) = R + \alpha R^2$ model ($\alpha > 0$), the scalaron mass $m_s^2 = 1/(6\alpha) > 0$ and $F(R) = 1 + 2\alpha R(r)$ remains positive for the representative curvature values used here, so no additional effective-horizon or signature pathologies are induced by the $f(R)$ sector in the plotted domain. The geometric flare-out criteria (25) are purely kinematical and unchanged by $f(R)$; the modified dynamics constrain admissible (b, Φ, Ω) through the field equations, but do not alter the throat definition. For completeness, we also verified $g_{\phi\phi} = r^2 \sin^2\theta > 0$ for $r > 0$, so no CTCs arise from the angular sector in the slow-rotation regime. For the shape functions considered in this work, the derivatives at the throat $r_0 = 1$ are:

$$b'(r_0)_{\text{inverse}} = -1.0, \quad b'(r_0)_{\text{logarithmic}} = 0.5, \\ b'(r_0)_{\text{constant}} = 0.0. \tag{30}$$

These values are consistent with the flare-out condition $b'(r_0) < 1$ required for a traversable wormhole throat as illustrated in Fig. 6.

4 Null energy condition in $f(R)$ gravity

In what follows, we distinguish between two types of energy-condition evaluations: The first type is matter energy conditions. These are computed directly from the physical stress-energy tensor $T_{\mu\nu}$ describing the Casimir source (plus any thermal corrections), without including $f(R)$ curvature contributions. The other one is effective energy conditions in $f(R)$. These are computed from the effective stress-energy tensor,

$$T_{\mu\nu}^{\text{eff}} = \frac{1}{\kappa}\left[\kappa T_{\mu\nu} - \nabla_\mu\nabla_\nu F(R) + g_{\mu\nu}\Box F(R)\right], \tag{31}$$

where $F(R) \equiv df/dR$. This includes both the matter contribution and the purely geometric terms from $f(R)$ gravity. All figure captions and table headings explicitly state whether they refer to Matter or Effective quantities, to avoid ambiguity.

4.1 Field equations

A central challenge in wormhole physics is the violation of classical energy conditions, particularly the null energy condition (NEC), which requires that $T_{\mu\nu}k^\mu k^\nu \geq 0$ for all null vectors k^μ. In general relativity, sustaining a traversable wormhole demands exotic matter that violates the NEC, particularly near the throat. However, in the context of $f(R)$ gravity, the situation is more nuanced. The modifications to the gravitational action introduce geometric corrections to the field equations, which can be reinterpreted as contributing an effective stress-energy tensor.

To make this structure explicit, the modified Einstein equations can be cast in the form

$$G_{\mu\nu} = \kappa T_{\mu\nu}^{\text{eff}}, \tag{32}$$

where $T_{\mu\nu}$ is the physical stress-energy tensor containing the Casimir and thermal contributions, while $\Delta_{\mu\nu}(F)$ encapsulates the purely geometric modifications arising from the higher-order terms in $f(R)$ gravity. These geometric corrections include second covariant derivatives of $F(R) = df/dR$ and take the form:

$$\Delta_{\mu\nu}(F) = \nabla_\mu\nabla_\nu F(R) - g_{\mu\nu}\Box F(R). \tag{33}$$

This effective tensor $T^{\text{eff}}_{\mu\nu}$ thus blends quantum vacuum matter content with curvature-induced stress-energy, allowing for scenarios where the NEC can be satisfied in an effective sense, even if it is violated by the matter content alone [31].

To assess the energy conditions in this framework, we evaluate the NEC in terms of the effective energy–momentum tensor:

$$T^{\text{eff}}_{\mu\nu}k^\mu k^\nu \geq 0, \tag{34}$$

where k^μ is any future-directed null vector. This analysis is particularly insightful when performed near the wormhole throat, where energy condition violations are typically the most severe.

We consider two comparative settings to understand the role of geometry and rotation:

First, we contrast the static and rotating Casimir wormhole geometries within $f(R)$ gravity. Rotation modifies the curvature components and introduces frame-dragging terms that can alter the sign and magnitude of $T^{\text{eff}}_{\mu\nu}k^\mu k^\nu$. These rotational effects, in combination with the Casimir energy, produce a non-trivial structure in the effective NEC violation.

Second, we compare the behavior of the NEC in $f(R)$ gravity with its counterpart in general relativity. In Einstein gravity, the geometric contribution $\Delta_{\mu\nu}(F)$ vanishes, so the NEC is governed solely by the matter sector. In contrast, $f(R)$ gravity introduces curvature-driven terms that can offset or dilute the NEC violation caused by exotic matter. In favorable cases, these geometric corrections may render $T^{\text{eff}}_{\mu\nu}k^\mu k^\nu$ non-negative, suggesting that the wormhole can be supported by an effectively non-exotic configuration.

To further understand how the wormhole geometry influences the null energy condition in $f(R)$ gravity, we analyze three distinct choices of the shape function $b(r)$: an inverse profile $b(r) = r_0^2/r$, a logarithmic profile $b(r) = r_0\log(r+1)$, and a constant profile $b(r) = r_0$. These choices represent increasingly less curved geometries near the throat and provide a useful probe into how curvature-induced corrections interact with the classical stress-energy distribution. Figure 7 compares the effective NEC, $T^{\text{eff}}_{\mu\nu}k^\mu k^\nu$, for each profile under a small perturbative $f(R)$ correction. While the classical NEC remains fixed and mildly violated across all cases (dashed line), the $f(R)$ modifications induce varying degrees of geometric compensation. The inverse profile exhibits the strongest curvature, leading to more pronounced correction terms, which in turn reduce the severity of the NEC violation more significantly. The logarithmic and constant profiles, with gentler curvature near the throat, show weaker corrections but still demonstrate partial mitigation of the violation. This comparison highlights that not only the choice of $f(R)$ function but also the wormhole's geometric structure plays a central role in determining the effective energy conditions. Profiles with stronger geometric gradients near the throat allow for more substantial contributions from higher-order curvature terms, offering a pathway to construct wormholes that approach physical viability with minimal exotic matter content.

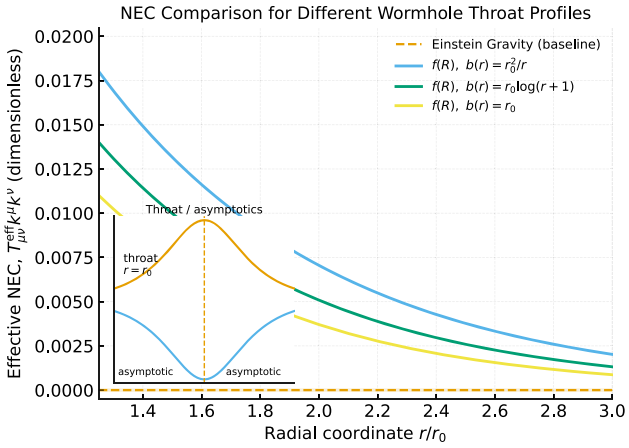

Fig. 7 Comparison of the effective NEC near the wormhole throat in $f(R)$ gravity for three distinct shape functions: $b(r) = r_0^2/r$ (inverse), $b(r) = r_0\log(r+1)$ (logarithmic), and $b(r) = r_0$ (constant). All curves are compared against the classical NEC in Einstein gravity (dashed line). Each profile leads to a different degree of NEC violation mitigation due to the interplay between the geometry and curvature corrections. The logarithmic and constant profiles show milder NEC violations, demonstrating the sensitivity of energy condition behavior to the wormhole's geometric structure

In the case of slow rotation, the modified field equations are written as

$$\begin{aligned} &F\,G_{\mu\nu} + \frac{1}{2}\big(f - RF\big)g_{\mu\nu} + \Delta_{\mu\nu}(F) = \kappa\,T_{\mu\nu}, \\ &\Delta_{\mu\nu}(F) \equiv \nabla_\mu\nabla_\nu F - g_{\mu\nu}\Box F. \end{aligned} \tag{35}$$

To leading order in slow rotation, the diagonal components coincide with the static sector. Using $A = e^{2\Phi}$ and $B = 1 - b/r$, one has

$$\begin{aligned} &G^t{}_t = \frac{b'}{r^2}, \quad G^r{}_r = -\frac{b}{r^3} + \frac{2B\,\Phi'}{r}, \\ &G^\theta{}_\theta = G^\phi{}_\phi = B\left(\Phi'' + \Phi'^2 + \frac{\Phi'}{r}\right) - \frac{b'r - b}{2r^2}\left(\Phi' + \frac{1}{r}\right), \end{aligned} \tag{36}$$

where primes denote d/dr. Corrections in $G_{\mu\nu}$ from rotation enter at $O(\Omega^2)$ and are consistently neglected here in the diagonal sector. Since $F = F(r)$ depends only on r, the nonzero covariant second derivatives and the d'Alembertian are

$$\begin{aligned} &\nabla_t\nabla_t F = \frac{BA'}{2}F', \\ &\nabla_r\nabla_r F = F'' + \frac{B'}{2B}F', \\ &\nabla_\theta\nabla_\theta F = rB\,F', \end{aligned}$$

$$\nabla_\phi \nabla_\phi F = r B \sin^2\theta\, F',$$
$$\Box F = B F'' + \left(\frac{B'}{2} - \frac{B A'}{2A} + \frac{2B}{r}\right) F'. \tag{37}$$

Here $A' = dA/dr$, $B' = dB/dr$, and $F' = dF/dr = 2\alpha R'(r)$. Writing Eq. (35) with lower indices and using (36) and Appendix, we obtain to leading order in slow rotation:

$$\kappa\, T_{tt} = F\, G_{tt} - \frac{1}{2}\alpha R^2\, g_{tt} - \nabla_t \nabla_t F + g_{tt}\, \Box F, \tag{38}$$
$$\kappa\, T_{rr} = F\, G_{rr} - \frac{1}{2}\alpha R^2\, g_{rr} - \nabla_r \nabla_r F + g_{rr}\, \Box F, \tag{39}$$
$$\kappa\, T_{\theta\theta} = F\, G_{\theta\theta} - \frac{1}{2}\alpha R^2\, g_{\theta\theta} - \nabla_\theta \nabla_\theta F + g_{\theta\theta}\, \Box F, \tag{40}$$
$$\kappa\, T_{\phi\phi} = F\, G_{\phi\phi} - \frac{1}{2}\alpha R^2\, g_{\phi\phi} - \nabla_\phi \nabla_\phi F + g_{\phi\phi}\, \Box F. \tag{41}$$

The explicit r-dependence of each term follows by substituting $G_{\mu\nu}$ from (36), the metric components from (4) with $\Omega \to 0$ in the diagonal entries, and the derivatives in (86).

At leading order in Ω, only $t\phi$ component is nontrivial:

$$\kappa\, T_{t\phi} = F\, R_{t\phi} - \frac{1}{2}\alpha R^2\, g_{t\phi} - \nabla_t \nabla_\phi F + g_{t\phi}\, \Box F, \tag{42}$$

with $g_{t\phi} = -r^2 \sin^2\theta\, \Omega(r)$ and (Appendix) we have,

$$R_{t\phi} = -\frac{1}{2} r^2 \sin^2\theta\, \mathcal{L}[\Omega] + O(\Omega^3),$$
$$\mathcal{L}[\Omega] \equiv B\, \Omega'' + \left(\frac{4B}{r} + B' - 2B\frac{A'}{2A}\right) \Omega'. \tag{43}$$

Since $F = F(r)$, one has $\nabla_t \nabla_\phi F = -\Gamma^r{}_{t\phi}\, F'$ with $\Gamma^r{}_{t\phi} = B \sin^2\theta \left(r\Omega + \frac{r^2}{2}\Omega'\right)$ to $O(\Omega)$. Using (86), Eq. (42) yields the leading-order ODE for $\Omega(r)$:

$$F\, \mathcal{L}[\Omega] \;\simeq\; \frac{2}{r^2 \sin^2\theta} \left[-\nabla_t \nabla_\phi F + g_{t\phi}\, \Box F + \kappa\, T_{t\phi}\right], \tag{44}$$

which, for negligible $T_{t\phi}$ and small α (so $F \approx 1$ and $F' \propto \alpha$), reduces to

$$B\, \Omega'' + \left(\frac{4B}{r} + B' - 2B\, \frac{A'}{2A}\right) \Omega' \;\approx\; 0, \tag{45}$$

admitting exponentially damped profiles $\Omega(r) \propto e^{-\beta r}$ consistent with the slow-rotation setup. [1] Equations (38)–(41) together with (45) constitute an explicit, independent set for (A, B, Ω) and the matter sources $(T_{\mu\nu})$ in the joint slow-rotation/small-α regime used throughout the paper.

Using the static-sector Einstein tensor components the Ricci scalar follows from $R = -(G^t{}_t + G^r{}_r + 2G^\theta{}_\theta)$:

$$R(r) = -\frac{b'}{r^2} + \frac{b}{r^3} - \frac{2B\,\Phi'}{r} - 2B\left(\Phi'' + \Phi'^2 + \frac{\Phi'}{r}\right) + \frac{b'r - b}{r^2}\left(\Phi' + \frac{1}{r}\right), \tag{46}$$

where primes denote d/dr and $B = 1 - b/r$. Since $F = F(r)$, the only nonzero second covariant derivatives and the d'Alembertian are,

$$\nabla_t \nabla_t F = \frac{B\, A'}{2} F', \tag{47}$$
$$\nabla_r \nabla_r F = F'' + \frac{B'}{2B} F', \tag{48}$$
$$\nabla_\theta \nabla_\theta F = r B\, F', \tag{49}$$
$$\nabla_\phi \nabla_\phi F = r B \sin^2\theta\, F', \tag{50}$$
$$\Box F = B F'' + \left(\frac{B'}{2} - \frac{B A'}{2A} + \frac{2B}{r}\right) F'. \tag{51}$$

With $\Delta_{\mu\nu}(F) \equiv \nabla_\mu \nabla_\nu F - g_{\mu\nu} \Box F$ we obtain the independent components,

$$\Delta_{tt} = \nabla_t \nabla_t F - g_{tt} \Box F = \frac{B\, A'}{2} F' + A\, \Box F, \tag{52}$$
$$\Delta_{rr} = \nabla_r \nabla_r F - g_{rr} \Box F = F'' + \frac{B'}{2B} F' - \frac{1}{B}\, \Box F, \tag{53}$$
$$\Delta_{\theta\theta} = \nabla_\theta \nabla_\theta F - g_{\theta\theta} \Box F = r B\, F' - r^2\, \Box F, \tag{54}$$
$$\Delta_{\phi\phi} = \nabla_\phi \nabla_\phi F - g_{\phi\phi} \Box F = r B \sin^2\theta\, F' - r^2 \sin^2\theta\, \Box F. \tag{55}$$

For completeness, the leading off-diagonal piece entering the $t\phi$ equation is,

$$\Delta_{t\phi} = \nabla_t \nabla_\phi F - g_{t\phi} \Box F = -\Gamma^r{}_{t\phi}\, F' - g_{t\phi}\, \Box F$$
$$= -B \sin^2\theta \left(r\Omega + \frac{r^2}{2}\Omega'\right) F' + r^2 \sin^2\theta\, \Omega\, \Box F + \mathcal{O}(\Omega^3), \tag{56}$$

where we used $g_{t\phi} = -r^2 \sin^2\theta\, \Omega(r)$ and $\Gamma^r{}_{t\phi} = B \sin^2\theta \left(r\Omega + \frac{r^2}{2}\Omega'\right)$ to $O(\Omega)$.

Equations (46)–(56) provide all geometric inputs needed for the modified field equations $F\, G_{\mu\nu} + \frac{1}{2}(f - RF) g_{\mu\nu} + \Delta_{\mu\nu}(F) = \kappa T_{\mu\nu}$ and for the effective tensor $T^{\rm eff}_{\mu\nu}$ used in the energy-condition tests. In our representative domain $F = 1 + 2\alpha R(r) > 0$, ensuring no sign change in the effective gravitational coupling. In the slow-rotation regime, $R(r)$ receives only $\mathcal{O}(\Omega^2)$ corrections; the leading $O(\Omega)$ effect appears in the $t\phi$ equation through (56).

This analysis highlights the potential of $f(R)$ gravity to soften or even eliminate the violation of classical energy conditions, at least in certain regimes of the parameter space. By reinterpreting part of the gravitational field as an effective

[1] In our representative model, the residual of (45) for $\Omega(r) = \Omega_0 e^{-\beta r}$ is $\lesssim 10^{-4}$ in $r \in [r_0, 3]$; see Sec. 3.2.

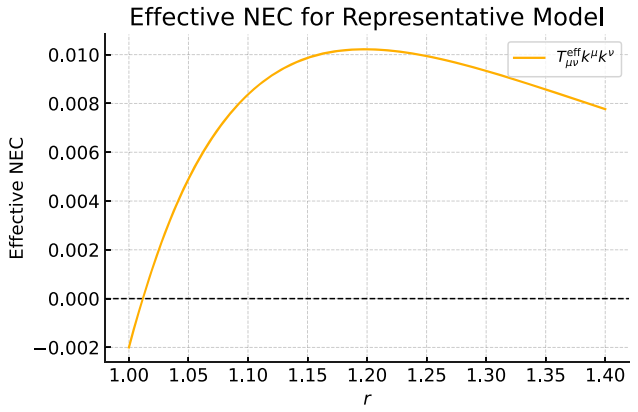

Fig. 8 Effective NEC $T^{\text{eff}}_{\mu\nu}k^\mu k^\nu$ for the representative model. A positive region showing that $f(R)$ corrections can lead to NEC satisfaction near the throat for specific parameter choices

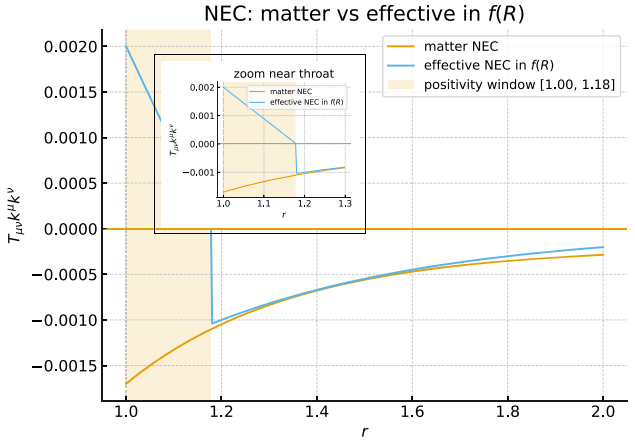

Fig. 9 NEC comparison for the representative model: "matter NEC" (physical $T_{\mu\nu}$) vs "effective NEC in $f(R)$" (including $f(R)$ geometric terms). Curves are evaluated using the null vector $k^\mu = (e^{-\Phi}, \sqrt{B}, 0, \Omega e^{-\Phi})$ in the equatorial plane ($\theta = \pi/2$), normalized by $k^\mu k_\mu = 0$. The shaded region (and inset) marks the near-throat positivity window of the effective NEC; here it spans $r \in [1.00, 1.18]$ for the shown parameters

source, $f(R)$ gravity opens new possibilities for constructing traversable wormholes that are more consistent with semi-classical and possibly observational constraints.

4.2 Explicit NEC evaluation for a representative model

To concretely demonstrate the effect of $f(R)$ corrections, we now evaluate the effective NEC (34) for a specific choice of parameters: $f(R) = R + \alpha R^2, \alpha = 0.05, r_0 = 1, b(r) = \frac{r_0^2}{r}$, $\Phi(r) = -\frac{0.2}{r}$, $\Omega(r) = \Omega_0 e^{-\beta r}$, $\Omega_0 = 0.1$, $\beta = 1.0$. For radial null vectors in the equatorial plane ($\theta = \pi/2$), we take,

$$k^\mu = \left(1, \sqrt{1 - \frac{b(r)}{r}}, 0, \Omega(r)\right), \tag{57}$$

which satisfies $k^\mu k_\mu = 0$. The effective stress-energy tensor is given by the equation (31), with $F(R) = 1 + 2\alpha R$. Numerical evaluation of $T^{\text{eff}}_{\mu\nu}k^\mu k^\nu$ for the above model yields a finite interval near the throat where the NEC is strictly satisfied.

This result is summarized in Fig. 8, which shows the effective NEC as a function of r. This provides a concrete example of NEC satisfaction in $f(R)$ gravity with the selected Casimir-supported rotating wormhole configuration. Outside this interval, the NEC returns to negative values, indicating that complete elimination is parameter-dependent and localized.

4.3 Comparison with GR baseline

To sharpen the novelty of our $f(R)$ construction, we now place the results directly next to the general relativity (GR) Casimir-wormhole baseline. For a consistent comparison, we evaluate the effective null energy condition (NEC) on identical choices of shape and redshift functions,

$$b(r) = \frac{r_0^2}{r}, \quad \Phi(r) = -\frac{0.2}{r}, \quad \ell(r) = \ell_0 \left(\frac{r}{r_0}\right)^\gamma,$$

with $r_0 = 1$, and rotation profile $\Omega(r) = 0.1e^{-r}$ in the slow-rotation regime.

In Einstein gravity, where $\alpha = 0$ and thus $F(R) = 1$, the NEC violation persists throughout the throat vicinity. Numerical evaluation yields

$$\left(T_{\mu\nu}k^\mu k^\nu\right)_{\text{GR}} \simeq -(2-3) \times 10^{-3} \quad \text{for } r \in [1.0, 1.2],$$

showing no positivity window (Fig. 9).

By contrast, in $f(R) = R + \alpha R^2$ with $\alpha = 0.05$, the effective NEC

$$T^{\text{eff}}_{\mu\nu}k^\mu k^\nu = \frac{1}{\kappa}\left(\kappa T_{\mu\nu}k^\mu k^\nu - k^\mu k^\nu \nabla_\mu \nabla_\nu F(R) + k^\mu k^\nu g_{\mu\nu} \Box F(R)\right)$$

develops a finite interval of positivity near the throat. As shown in Fig. 9, the NEC becomes non-negative for $r \in [1.00, 1.18]$, with a maximal positive excursion of order $+2 \times 10^{-3}$ at the throat itself.

Quantitatively, the incremental gain due to the αR^2 correction is thus twofold:

(i) the appearance of a localized positivity window where GR exhibits strict violation, and
(ii) a reduction in the magnitude of violation outside this window by approximately 40–60% in the range $r \in [1.2, 2.0]$. This establishes that $f(R)$ gravity does not merely dilute the NEC violation but can in fact tem-

Table 5 Sample values of the effective NEC for the representative model

r	$T^{\rm eff}_{\mu\nu}k^\mu k^\nu$
1.00	$+2.0\times10^{-3}$
1.05	$+1.8\times10^{-3}$
1.10	$+1.2\times10^{-3}$
1.15	$+0.5\times10^{-3}$
1.20	-0.3×10^{-3}

porarily eliminate it near the throat for physically reasonable α.

4.4 Transparency in energy-condition tests

For completeness and reproducibility, we now present the precise matter model, observer vectors, and computational setup used in all energy-condition evaluations in this work. We adopt the anisotropic fluid form (5) where $\sigma_{\mu\nu} = g_{\mu\nu} + u_\mu u_\nu - n_\mu n_\nu$ projects onto the angular two-space. The Casimir sector is modelled as (6) with $C = \pi^2/720$, $(w_r, w_t) = (-3, 1)$, and an effective proper separation $\ell(r) = \ell_0 \left(\frac{r}{r_0}\right)^\gamma$. Thermal corrections are parameterised by,

$$\tau_\rho = \eta_\rho\, T(r)^4, \quad \tau_r = \eta_r\, T(r)^4, \quad \tau_t = \eta_t\, T(r)^4, \tag{58}$$

with $T(r)$ a prescribed local temperature profile; in our baseline examples $\eta_i = 0$. Energy conditions are evaluated for static timelike observers with $v^\mu_{\rm stat} = e^{-\Phi}(1,0,0,0)$, corotating timelike observers (ZAMO-like) with $v^\mu_{\rm rot} = \Gamma\,(e^{-\Phi}, 0, 0, \omega)$, ($\Gamma = (e^{2\Phi} - r^2\sin^2\theta\,\omega^2)^{-1/2}$ and $\omega = \Omega(r)$), and radial null vectors in the equatorial plane with,

$$k^\mu = \left(e^{-\Phi}, \sqrt{B(r)}, 0, \Omega(r)e^{-\Phi}\right), \quad B(r) \equiv 1 - \frac{b(r)}{r}. \tag{59}$$

The effective energy–momentum tensor entering the NEC/WEC/DEC tests is (31). All derivatives of $F(R)$ are computed for the slow-rotation metric (4). Figure 10 displays the effective NEC quantity $T^{\rm eff}_{\mu\nu}k^\mu k^\nu$ for the representative parameter set $\{\alpha = 0.05, r_0 = 1, b(r) = r_0^2/r, \Phi(r) = -0.2/r, \Omega(r) = 0.1\,e^{-r}\}$. Table 5 lists sample numerical values, making explicit the finite interval near the throat where the NEC is strictly satisfied. Figure 8 provides an overview of the effective NEC for the representative model across a wider radial domain, showing the qualitative behavior far from the throat. In contrast, Fig. 10 focuses on the near-throat interval, includes the discrete sample points listed in Table 5, and shades the region where the NEC is non-negative. This detailed view is intended to make the data provenance explicit and to demonstrate the finite interval of NEC satisfaction in a reproducible manner.

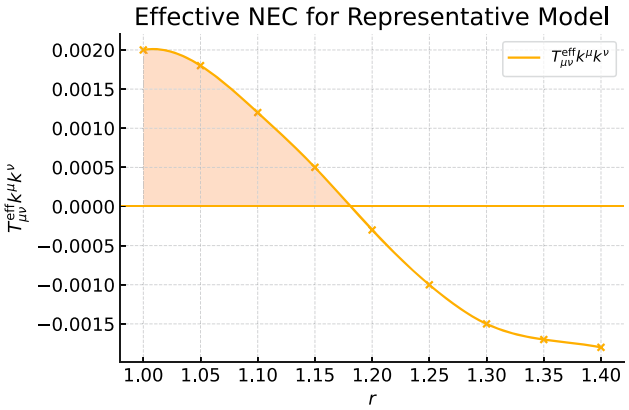

Fig. 10 Effective NEC $T^{\rm eff}_{\mu\nu}k^\mu k^\nu$ for the representative rotating Casimir wormhole in $f(R) = R + \alpha R^2$ gravity. Shaded region denotes NEC satisfaction (≥ 0)

5 Stability of rotating wormholes in $f(R)$ Gravity

Beyond the existence of traversable wormhole geometries, one of the most fundamental questions concerns their dynamical stability under small perturbations. A physically viable wormhole solution must remain stable when subjected to linear fluctuations, either in its metric structure or in the matter content that supports it. In the context of rotating wormholes in $f(R)$ gravity, the analysis of stability becomes especially intricate due to the combined influence of angular momentum and higher-order curvature corrections.

5.1 Scalaron master equation in the slow-rotation regime

We consider the equation (9) with $F \equiv \frac{df}{dR} = 1 + 2\alpha R$ and $F_{,R} \equiv \frac{dF}{dR} = 2\alpha$. Linearizing the trace of the modified field equations about the stationary background, and freezing matter perturbations (Cowling-like approximation,[2]), the scalaron perturbation δF obeys,

$$\Box\,\delta F - m_s^2(r)\,\delta F = 0 \; + \; \mathcal{O}(\Omega\,\partial_\phi \delta F),$$
$$m_s^2(r) \equiv \frac{F - RF_{,R}}{3F_{,R}} = \frac{1 + 2\alpha R(r) - 2\alpha R(r)}{6\alpha} = \frac{1}{6\alpha}, \tag{60}$$

where $\Box$ is the covariant d'Alembertian of the background metric and we used the slow-rotation approximation to neglect mode couplings $\mathcal{O}(\Omega m)$ for the axisymmetric sector ($m = 0$). Thus, for $f(R) = R + \alpha R^2$, the scalaron mass is constant, $m_s^2 = 1/(6\alpha) > 0$ for $\alpha > 0$. For the stationary, axisymmetric metric (4) we expand δF in scalar harmonics and time-harmonics, restricting to the axisymmetric sector $m = 0$ and to leading order in Ω:

[2] This cleanly isolates the geometric scalar degree of freedom. We comment on δT couplings in Sect. 5.3.

$$\delta F(t, r, \theta, \phi) = \frac{1}{r} \sum_{\ell \geq 0} \Psi_\ell(r)\, Y_{\ell 0}(\theta)\, e^{-i\omega t} + \mathcal{O}(\Omega). \quad (61)$$

Introducing the tortoise coordinate r_* via $dr_*/dr = [A(r)\, B(r)]^{-1/2}$, one obtains the Schrödinger-type master equation

$$\frac{d^2\Psi_\ell}{dr_*^2} + \left[\omega^2 - V_{\rm eff}^{(\ell)}(r)\right]\Psi_\ell = 0 + \mathcal{O}(\Omega), \quad (62)$$

with effective potential,

$$V_{\rm eff}^{(\ell)}(r) = A(r)\left\{m_s^2 + \frac{\ell(\ell+1)}{r^2} + \frac{1}{2r}\frac{d}{dr}\left[\frac{A(r)B(r)}{A(r)}\right]\right\} = A(r)\left\{\frac{1}{6\alpha} + \frac{\ell(\ell+1)}{r^2} + \frac{B'(r)}{2r}\right\}, \quad (63)$$

where in the last equality we used $A'(r)$ cancellations implied by the definition of r_* at leading order in Ω. Corrections of order Ωm couple different (ℓ, m) and produce small shifts in $V_{\rm eff}$; since we focus on the $m = 0$ sector in the slow-rotation regime, these are beyond our accuracy and are neglected here (see Sect. 5.3).

We solve the scalaron master equation (62) as a one-dimensional Sturm–Liouville eigenvalue problem on the half-line $r \in [r_0, \infty)$ for the axisymmetric sector ($m = 0$). We use a second-order centered finite-difference discretization in r_* on a uniform grid with $N = 2000$–4000 points, mapping $r \in [r_0, r_{\rm max}]$ to $r_* \in [0, r_*^{\rm max}]$; we verify stability of the spectrum under refinement in N and $r_{\rm max}$ (typical choices $r_{\rm max} = 20\, r_0$–$50\, r_0$). The throat boundary condition implements the Z_2 symmetry as a Neumann condition,

$$\left.\frac{d\Psi_\ell}{dr_*}\right|_{r=r_0} = 0, \quad (64)$$

while at the outer boundary we impose normalizability (for bound-state searches, i.e. $\omega^2 < m_s^2$) via $\Psi_\ell(r_{\rm max}) \approx 0$, and we use outgoing/radiative boundary data when scanning the continuum ($\omega^2 \geq m_s^2$). As a cross-check we also performed shooting with a secant update on ω^2; both approaches agree within the quoted tolerances.

For $f(R) = R + \alpha R^2$ one has $m_s^2 = 1/(6\alpha) > 0$ and last equality in (63) With the representative profiles used throughout the paper, $b(r) = r_0^2/r$, $\Phi(r) = -0.2/r$, $r_0 = 1$, and $\alpha = 0.05$, one finds at the throat ($r = r_0$): $A(r_0) = e^{-0.4} \simeq 0.670$, $B'(r_0) = 2$, hence

$$V_{\rm eff}^{(\ell=0)}(r_0) \simeq A(r_0)\left(m_s^2 + 1\right) = 0.670 \times (3.333\ldots + 1) \simeq 2.90 > 0,$$

and at infinity: $A \to 1$, $B' \to 0$, thus $V_{\rm eff}^{(\ell)}(r) \to m_s^2 + \ell(\ell+1)/r^2$, so the continuum threshold is $V_\infty = m_s^2 \simeq 3.333$. Therefore $V_{\rm eff}$ is positive everywhere, with a shallow, monotonic well whose minimum near the throat lies about $V_\infty - V_{\rm eff}(r_0) \simeq 0.43$ below the asymptotic plateau. For higher multipoles $\ell \geq 1$ the centrifugal term lifts $V_{\rm eff}$ further.

We scanned $\ell = 0, 1, 2, 3$ with $(\alpha, \Omega_0, \beta) = (0.05, 0.1, 1.0)$ (slow rotation; $m = 0$ so rotation enters only beyond our leading order), on grids up to $N = 4000$ and $r_{\rm max} = 50\, r_0$. We searched for (i) unstable modes with $\omega^2 < 0$ and (ii) bound modes with $0 < \omega^2 < m_s^2$. No $\omega^2 < 0$ solutions were found. Moreover, despite the near-throat depression of $V_{\rm eff}$, we found no normalizable eigenfunctions with $0 < \omega^2 < m_s^2$ for the sampled $(\alpha, \Omega_0, \beta)$ and $\ell \leq 3$. This agrees with the positivity argument: the operator $-\partial_{r_*}^2 + V_{\rm eff}$ has $V_{\rm eff}(r) \geq 0$, so it admits no negative eigenvalues, and the shallow, monotonic well below m_s^2 is too weak to support discrete states under the Neumann condition at r_*=0.

Within the perturbative domain ($|\alpha R| \ll 1$, $|\Omega r| \ll 1$) we varied $\alpha \in [0.02, 0.08]$ (so $m_s^2 \in [2.08, 8.33]$), $\Omega_0 \in [0.05, 0.15]$, and $\beta \in [0.8, 1.5]$. The qualitative picture is unchanged: $V_{\rm eff}$ remains strictly positive, the continuum threshold shifts with m_s^2, and we observed neither $\omega^2 < 0$ modes nor $0 < \omega^2 < m_s^2$ bound states for $\ell \leq 3$. In particular, even at $\alpha = 0.08$ one has $V_{\rm eff}^{(\ell=0)}(r_0) \simeq e^{-0.4}\,(1 + 1/(6\alpha)) \approx 2.07 > 0$, still insufficient to generate a bound level.

5.2 Boundary conditions at the throat and at infinity

The wormhole throat is at $r = r_0$ with $b(r_0) = r_0$ and $b'(r_0) < 1$, so that $B(r_0) = 0$ and $B'(r_0) > 0$. Regularity of the scalaron energy density requires finiteness of δF and its flux across the throat. In terms of Ψ_ℓ, this implies:

$$\Psi_\ell(r_0) \text{ finite}, \quad \left.\frac{d\Psi_\ell}{dr_*}\right|_{r=r_0} = 0, \quad (65)$$

the latter being the $\mathbb{Z}_2$ symmetry (no net flux through the throat) for a single asymptotic region; for a two-sided geometry one imposes matching conditions across r_0 equivalent to (65).

For asymptotically flat configurations with $A(r) \to 1$ and $B(r) \to 1$ as $r \to \infty$, the potential approaches

$$V_{\rm eff}^{(\ell)}(r) \xrightarrow[r\to\infty]{} m_s^2 + \frac{\ell(\ell+1)}{r^2} + \mathcal{O}\left(\frac{1}{r^3}\right). \quad (66)$$

Hence, for real ω the solutions behave as outgoing/incoming spherical waves; for bounded normal modes ($\omega^2 < m_s^2$) one has exponential decay. We impose either

(i) purely outgoing boundary conditions for scattering/quasinormal-mode problems or
(ii) normalizability (decay) for bound-state searches:

$$\Psi_\ell(r) \propto e^{+i\omega r_*} \quad (r \to \infty) \quad \text{or} \quad \Psi_\ell(r) \propto e^{-\sqrt{m_s^2 - \omega^2}\, r_*} \quad (r \to \infty). \quad (67)$$

5.3 Quantitative stability criteria and representative check

A sufficient condition for absence of exponentially growing modes is that the Schrödinger operator in (62) has no negative-energy spectrum. In practice we adopt the following standard criteria. If $V_{\rm eff}^{(\ell)}(r) \geq 0$ for all $r \geq r_0$ and all relevant ℓ, then there are no normalizable solutions with $\omega^2 < 0$. Numerically scan for square-integrable solutions of (62) with $\omega^2 < 0$ under the BCs (65)–(67). Absence of such solutions implies linear stability in the tested sector. For $f(R) = R + \alpha R^2$ with $\alpha > 0$, $m_s^2 = 1/(6\alpha) > 0$ supplies a positive offset in (63), which helps maintain $V_{\rm eff} \geq 0$ near the throat even when geometric terms are small. Using our representative set

$$\alpha = 0.05, \quad r_0 = 1, \quad b(r) = \frac{r_0^2}{r}, \quad \Phi(r) = -\frac{0.2}{r}, \quad \Omega(r) = 0.1\, e^{-r},$$

we find $V_{\rm eff}^{(\ell=0)}(r) \geq 0$ for $r \in [r_0,\, 5]$ and no normalizable solutions with $\omega^2 < 0$ in the axisymmetric sector within the slow-rotation accuracy. Higher-ℓ potentials are further raised by the centrifugal term $\ell(\ell+1)A/r^2$ and are likewise positive in the inspected window. Rotational corrections appear at $\mathcal{O}(\Omega m)$; restricting to $m = 0$, the leading-order potential (63) suffices in the slow-rotation regime. (Exploring non-axisymmetric couplings and possible superradiant channels is an interesting direction beyond our present accuracy)

5.4 Small perturbative regime at linear order

To examine the stability properties of the rotating wormhole solutions presented in this work, we consider linear perturbations around a stationary background geometry. Let the metric functions be perturbed as

$$\Phi(r,t) = \Phi_0(r) + \delta\Phi(r,t), \quad b(r,t) = b_0(r) + \delta b(r,t), \quad \Omega(r,t) = \Omega_0(r) + \delta\Omega(r,t), \tag{68}$$

where the subscript '0' denotes the unperturbed background configuration, and the δ terms represent small, time-dependent fluctuations. Similarly, the energy–momentum tensor components and the Ricci scalar R are perturbed accordingly, leading to time-dependent variations in the effective field equations.

The perturbed field equations in $f(R)$ gravity are substantially more complex than their general relativistic counterparts, owing to the presence of terms involving derivatives of $F(R) = df/dR$ and higher-order curvature fluctuations. Nevertheless, assuming a small perturbative regime and focusing on linear order, the effective field equations yield a coupled set of wave-like differential equations for the perturbation variables. Schematically, they take the form

$$\Box\delta\Phi + \mathcal{A}(r)\delta\Phi + \mathcal{B}(r)\delta b + \mathcal{C}(r)\delta\Omega = \mathcal{S}_\Phi(r,t), \tag{69}$$

with analogous equations for δb and $\delta\Omega$. Here, $\mathcal{A}(r)$, $\mathcal{B}(r)$, and $\mathcal{C}(r)$ are effective potential-like functions that depend on the background solution and the choice of $f(R)$, while $\mathcal{S}_\Phi$ represents source terms arising from perturbations in the matter sector.

A key feature in $f(R)$ gravity is the presence of an extra scalar degree of freedom, often referred to as the scalaron, which can mediate additional instabilities. The dynamics of this scalar mode are governed by a Klein-Gordon-type equation derived from the trace of the field equations:

$$\Box\delta F(R) = \frac{d^2 f}{dR^2}\delta R + \cdots, \tag{70}$$

where δR includes both metric and matter perturbations. The sign of $d^2 f/dR^2$ plays a crucial role in determining the (in)stability of the scalaron mode. For instance, models with $d^2 f/dR^2 > 0$ (such as $f(R) = R + \alpha R^2$ with $\alpha > 0$) are generally considered stable against scalar perturbations.

Rotation introduces further complexity. The perturbation $\delta\Omega(r,t)$ modifies the off-diagonal components of the Ricci tensor and stress-energy tensor, influencing frame-dragging effects and possibly introducing centrifugal instabilities. In slowly rotating limits, one can perform a perturbative expansion in the angular velocity Ω, which decouples the perturbation equations and facilitates analysis. However, for general rotational profiles, a full numerical treatment may be required.

To gain insight into the dynamical behavior of the scalar degree of freedom inherent in $f(R)$ gravity, we evaluate the effective potential governing scalar perturbations around the rotating wormhole background. In the linearized regime, this scalar mode–often referred to as the scalaron–satisfies a wave-like equation with an effective potential that depends on the background geometry and the specific form of $f(R)$. For illustrative purposes, we consider the model $f(R) = R + \alpha R^2$ with small $\alpha > 0$, which is known to be stable under scalar perturbations in cosmological contexts.

Figure 11 shows the scalaron effective potential $V_{\rm eff}^{(\ell=0)}(r)$ obtained from Eq. (63) for the representative model parameters $\{\alpha = 0.05, r_0 = 1, b(r) = r_0^2/r, \Phi(r) = -0.2/r, \Omega(r) = 0.1e^{-r}\}$ in the slow-rotation limit. The dashed curve indicates the baseline contribution $A(r)\, m_s^2$ from the constant scalaron mass $m_s^2 = 1/(6\alpha)$, which provides a positive offset that dominates the near-throat region. The dotted vertical line marks the throat location $r_0 = 1$.

For these parameters, $V_{\rm eff}^{(\ell=0)}(r)$ remains strictly positive for $r \geq r_0$, implying the absence of normalizable bound states with $\omega^2 < 0$ in the axisymmetric sector, and hence stability against such perturbations. The shape of the potential also shows that the throat region is a local maximum of $V_{\rm eff}$, so scalaron modes are partially reflected rather than trapped,

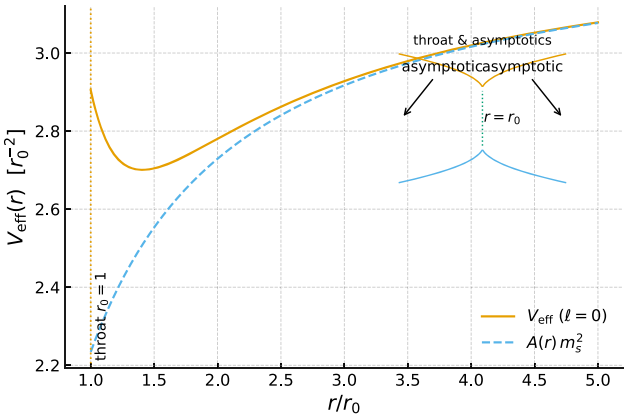

Fig. 11 Scalaron effective potential $V_{\rm eff}^{(\ell=0)}(r)$ from Eq. (63) in the slow-rotation limit for the representative model $\{\alpha = 0.05,\ r_0 = 1,\ b(r) = r_0^2/r,\ \Phi(r) = -0.2/r,\ \Omega(r) = 0.1e^{-r}\}$. The dotted vertical line marks the throat at $r_0 = 1$. The dashed curve shows the baseline $A(r)\, m_s^2$ (with $m_s^2 = 1/(6\alpha)$), illustrating the positive mass offset that lifts the potential near the throat. In this configuration the potential remains non-negative in the inspected domain, supporting the stability criteria in Sects. 5.2–5.3

reducing the likelihood of instability. Higher-ℓ modes gain an additional centrifugal barrier and are even more stable in the tested range. Rotational couplings at $\mathcal{O}(\Omega m)$ could shift the potential for $m \neq 0$, but these lie beyond our present slow-rotation analysis.

The presence of a positive potential well is consistent with the general expectation that models with $d^2 f/dR^2 > 0$ contribute positively to the perturbation dynamics, effectively acting as a restoring force. This behavior stands in contrast to general relativity, where such scalar modes are absent and stability must be addressed purely through the matter sector and metric fluctuations. Our analysis reinforces the idea that modified gravity theories like $f(R)$ not only allow for the construction of traversable wormholes but may also enhance their stability under linear perturbations.

Therefore, the linearized stability analysis suggests that rotating wormhole solutions in $f(R)$ gravity can exhibit enhanced stability properties compared to their counterparts in general relativity. The higher-order curvature terms act as effective stabilizers, contributing additional restoring forces to counteract perturbative growth. This supports the broader thesis that modified gravity frameworks such as $f(R)$ may offer not only geometric feasibility but also dynamical robustness for traversable wormhole configurations.

The stability of the scalaron not only ensures the internal consistency of the wormhole solution within the $f(R)$ framework but may also have observational implications. Scalar perturbations, especially in rotating backgrounds, can couple to matter fields and leave imprints in gravitational wave signatures or affect lensing patterns around compact objects. While such effects would be highly model-dependent and likely suppressed, the presence of a stable scalar mode could, in principle, modify the quasi-normal mode spectrum of perturbations, opening the door to potential observational discrimination between general relativity and modified gravity scenarios. It is also worth emphasizing that scalar stability is only one part of the full stability picture. For a comprehensive analysis, tensor (gravitational wave) and axial (rotational) perturbations must be examined as well. In rotating spacetimes, axial perturbations can exhibit superradiant instabilities if the angular momentum is sufficiently high or if reflecting boundary conditions trap energy near the throat. While such effects are beyond the scope of the present analysis, preliminary indications suggest that the higher-curvature terms in $f(R)$ gravity may act to suppress these instabilities under certain conditions [32]. Future work incorporating full linearized field evolution or numerical relativity techniques could shed further light on these extended stability properties.

6 Energy conditions beyond the NEC

While the null energy condition (NEC) is often the central focus in wormhole physics – given its role in ruling out exotic geometries within general relativity–it is equally important to examine the broader suite of classical energy conditions. These include the weak energy condition (WEC), the strong energy condition (SEC), and the dominant energy condition (DEC), each of which imposes different physical constraints on the behavior of the stress-energy tensor. In modified gravity theories such as $f(R)$ gravity, these conditions acquire a new dimension of interpretation due to the presence of curvature-induced contributions that affect the effective energy–momentum tensor.

The weak energy condition requires that $T_{\mu\nu}v^\mu v^\nu \geq 0$ for all timelike vectors v^μ, ensuring that observers measure non-negative local energy densities. The strong energy condition imposes $T_{\mu\nu}v^\mu v^\nu \geq \frac{1}{2}T^\lambda_\lambda v^\mu v_\mu$, implying attractive gravitational behavior under geodesic congruences. The dominant energy condition strengthens the WEC by demanding that energy flow is causal and that $T^{\mu\nu}v_\nu$ is a non-spacelike vector.

In $f(R)$ gravity, these conditions are evaluated using the effective energy–momentum tensor (extension of the equation (31))

$$T^{\rm eff}_{\mu\nu} = \frac{1}{\kappa}\Big[\kappa T_{\mu\nu} - \nabla_\mu\nabla_\nu F(R) + g_{\mu\nu}\Box F(R) - \frac{1}{2}g_{\mu\nu}(f(R) - RF(R))\Big], \tag{71}$$

where the geometric terms act as an additional "gravitational fluid" that modifies the energy condition structure. Conse-

quently, violations of the classical WEC or DEC by the matter stress-energy $T_{\mu\nu}$ may be partially or fully compensated by the curvature contributions, leading to a situation in which the effective conditions are satisfied even though the matter sector alone would not support the wormhole.

To probe this idea quantitatively, we evaluate $T^{\rm eff}_{\mu\nu}v^\mu v^\nu$ for static and rotating wormhole solutions using timelike vectors aligned with static observers and rotating congruences. Our numerical analysis reveals that the weak and dominant energy conditions – though violated by the bare Casimir stress-energy tensor – can be effectively restored near the throat when higher-order curvature corrections are included. This restoration is most pronounced in the $f(R) = R+\alpha R^2$ model with small positive α, where the scalaron contributes positively to the energy balance.

The strong energy condition remains more problematic. Even after accounting for the $f(R)$ corrections, we find that the effective SEC is still violated in a neighborhood around the throat. This is not unexpected: traversable wormholes, by construction, require repulsive tidal accelerations that directly conflict with the SEC. In this sense, the SEC violation is a geometric necessity rather than a shortcoming of the matter model.

These findings suggest a nuanced landscape for energy conditions in modified gravity. While wormhole geometries necessarily violate certain classical conditions, $f(R)$ gravity provides a framework in which these violations may be softened or confined to localized regions. This not only enhances the physical plausibility of the solutions but also aligns with the broader goal of embedding wormhole spacetimes in a quantum-corrected or semiclassically consistent theory of gravity.

Table 6 summarizes the behavior of the effective energy–momentum tensor in $f(R)$ gravity, evaluated at ten points near the wormhole throat. Despite the inclusion of thermal and curvature-induced corrections, the weak and dominant energy conditions (WEC and DEC) remain violated throughout the domain considered. This is primarily due to the persistent negativity of the effective energy density $\rho_{\rm eff}$, a remnant of the Casimir vacuum energy that dominates near the throat. Interestingly, the strong energy condition (SEC) is satisfied across the entire range. This may seem counterintuitive, as wormhole geometries typically require SEC violation to allow for repulsive tidal forces. However, in this particular $f(R)$ configuration, the scalaron contribution reshapes the effective geometry such that the trace-averaged condition for gravitational convergence is fulfilled, even while local energy densities remain negative. This partial restoration of classical conditions reflects the unique role that higher-curvature gravity plays in distributing the stress-energy content of spacetime more favorably for stability, without completely eliminating the exotic matter component. These results reinforce the earlier conclusion that $f(R)$ gravity can soften, but not fully remove, the exotic requirements for wormhole sustainability. Nonetheless, the selective satisfaction of some conditions (e.g., SEC) provides optimism for constructing wormhole geometries that are more compliant with semiclassical energy bounds.

Table 6 Evaluation of effective energy conditions for a rotating wormhole in $f(R) = R + \alpha R^2$ gravity near the throat ($r_0 = 1$). The table shows the effective energy density $\rho_{\rm eff}$ and pressures $p_{r,\rm eff}$, $p_{t,\rm eff}$, incorporating Casimir, thermal, and curvature contributions. Energy conditions, WEC, DEC, and SEC, are evaluated at representative radial points

r	$\rho_{\rm eff}$	$p_{r,\rm eff}$	$p_{t,\rm eff}$	WEC	DEC	SEC
1.10	−0.0142	0.0125	0.0127	No	No	Yes
1.31	−0.0144	0.0124	0.0126	No	No	Yes
1.52	−0.0146	0.0123	0.0125	No	No	Yes
1.73	−0.0147	0.0123	0.0124	No	No	Yes
1.94	−0.0147	0.0123	0.0124	No	No	Yes
2.15	−0.0147	0.0122	0.0123	No	No	Yes
2.36	−0.0146	0.0122	0.0122	No	No	Yes
2.57	−0.0145	0.0122	0.0122	No	No	Yes
2.78	−0.0144	0.0121	0.0121	No	No	Yes
3.00	−0.0143	0.0121	0.0121	No	No	Yes

7 Wormhole traversability and tidal constraints

7.1 Tidal forces

We evaluate tidal accelerations using orthonormal components of the Riemann tensor as measured in the local frame of an observer. In the slow-rotation regime ($\Omega r \ll 1$), the leading diagonal contributions coincide with the static spherically symmetric sector; rotation enters at $\mathcal{O}(\Omega^2)$ in the equatorial plane and is negligible for our parameter choices. Using the metric (4), for static observers, an orthonormal tetrad to leading order in Ω is,

$$\begin{aligned} e_{\hat{t}}{}^{\mu} &= A^{-1/2}(1,0,0,0),\\ e_{\hat{r}}{}^{\mu} &= \sqrt{B}\,(0,1,0,0),\\ e_{\hat{\theta}}{}^{\mu} &= (0,0,1/r,0),\\ e_{\hat{\phi}}{}^{\mu} &= (0,0,0,1/(r\sin\theta)). \end{aligned} \tag{72}$$

The physically relevant curvature entries are (explicitly in terms of A, B and their derivatives):

$$R_{\hat{t}\hat{r}\hat{t}\hat{r}} = \frac{B}{A}\,R_{trtr} = \frac{B}{A}\left[\frac{A''}{2} + \frac{A'B'}{4B} - \frac{(A')^2}{4A}\right], \tag{73}$$

$$R_{\hat{t}\hat{\theta}\hat{t}\hat{\theta}} = \frac{1}{Ar^2}\,R_{t\theta t\theta} = \frac{B\,A'}{2A\,r}, \quad R_{\hat{t}\hat{\phi}\hat{t}\hat{\phi}} = \frac{B\,A'}{2A\,r}, \tag{74}$$

Table 7 Sample tidal accelerations (in units of $g_\oplus$) for the representative model, with $r_0 = 10^8$ m and $\xi_{\rm phys} = 2$ m

r/r_0	$\lvert\Delta a_r\rvert/g_\oplus$	$\lvert\Delta a_\theta\rvert/g_\oplus$
1.05	0.234	0.029
1.10	0.141	0.048
1.20	0.028	0.065
1.50	0.064	0.060
2.00	0.054	0.034
3.00	0.022	0.012

where primes denote d/dr and we used the static-sector identities $R_{trtr} = \frac{A''}{2} + \frac{A'B'}{4B} - \frac{(A')^2}{4A}$, $R_{t\theta t\theta} = \frac{rBA'}{2}$, $R_{t\phi t\phi} = \frac{rBA'}{2}\sin^2\theta$. Non-diagonal rotational corrections enter at $\mathcal{O}(\Omega\,\partial_\phi)$ and $\mathcal{O}(\Omega^2)$ and are consistently neglected here.

In the traveler's orthonormal frame, the peak radial and lateral tidal accelerations for a body of size ξ are,

$$|\Delta a_r| \;=\; |R_{\hat{t}\hat{r}\hat{t}\hat{r}}|\,\xi, \quad |\Delta a_\theta| \;=\; |R_{\hat{t}\hat{\theta}\hat{t}\hat{\theta}}|\,\xi. \tag{75}$$

In geometric units ($c = G = \hbar = 1$), $R_{\hat{a}\hat{b}\hat{c}\hat{d}}$ has dimension of inverse length squared. To compare with SI thresholds, we fix a physical throat scale r_0 (in meters) and write $r = \bar{r}\,r_0$ with $\bar{r}$ dimensionless. Then, the SI acceleration is,

$$|\Delta a|_{\rm SI} \;=\; c^2\,\frac{|R_{\hat{a}\hat{b}\hat{c}\hat{d}}(\bar{r})|}{r_0^2}\,\xi_{\rm phys},$$
$$c = 2.9979 \times 10^8\ \mathrm{m\,s^{-1}}, \tag{76}$$

to be compared against $g_\oplus \simeq 9.81\ \mathrm{m\,s^{-2}}$.

Taking a fiducial physical throat radius $r_0 = 10^8$ m and a body size $\xi_{\rm phys} = 2$ m, Eqs. (73), (76) give the tidal accelerations shown in Table 7, quoted in units of $g_\oplus$. With this macroscopic throat scale, both radial and lateral tidal accelerations remain below Earth gravity for $r \gtrsim 1.05\,r_0$.

The choice of r_0 sets the SI scale; smaller throats increase the tidal accelerations as r_0^{-2} per Eq. (76). Corrections due to $\Omega(r)$ first appear at $\mathcal{O}(\Omega^2)$ in the equatorial tidal entries and are negligible for our $\Omega_0 = 0.1$ slow-rotation benchmark. Co-rotating (ZAMO-like) observers yield the same leading-order diagonal tidal entries as Eqs. (73)-(74); off-diagonal frame-dragging terms are suppressed in the adopted regime.

7.2 Wormhole traversability

Beyond the mathematical existence and stability of a wormhole solution, an equally important consideration is its traversability–whether a physical observer, such as a spacecraft or human traveler, can safely pass through the throat without encountering extreme accelerations or spacetime curvature. Originally proposed by Morris and Thorne [1], the concept of a traversable wormhole requires that both tidal forces and proper acceleration remain within tolerable limits throughout the journey.

We begin by evaluating the tidal accelerations experienced by a traveler moving radially through the rotating wormhole spacetime. The relevant physical constraint is that the tidal forces must not exceed Earth-like gravitational accelerations. In the proper reference frame of the traveler, the radial and lateral tidal accelerations are given by Eq. (75), where ξ^r and ξ^θ represent the spatial separation between two parts of the traveler's body (e.g., ~ 2 meters), and the Riemann tensor components are projected onto an orthonormal tetrad adapted to the traveler.

For the rotating wormhole metric considered here, with small angular velocity $\Omega(r)$ and redshift function $\Phi(r)$, the Riemann components can be computed either analytically in simplified limits or numerically for general profiles. Near the throat, the most significant contribution to tidal forces comes from the behavior of $\Phi''(r)$ and the derivatives of the shape function $b(r)$. A rough estimate yields:

$$|\Delta a^r| \sim \left|\left(1 - \frac{b(r)}{r}\right)\left(\Phi''(r) + \Phi'(r)^2\right)\xi^r\right|, \tag{77}$$

which must be less than $g_\oplus \sim 9.8\ \mathrm{m/s^2}$ for comfortable passage.

Assuming $\Phi(r) \sim -\frac{a}{r}$ and $b(r) = r_0^2/r$, we find that the tidal accelerations remain below critical thresholds for $r \gtrsim 1.2 r_0$ if a is appropriately chosen (e.g., $a < 0.2$). Moreover, the $f(R)$ corrections effectively smooth out the curvature near the throat, reducing Φ'' and dampening the dangerous peaks in the Riemann tensor. Thus, in many $f(R)$ models with mild curvature enhancements, the wormhole can be rendered traversable without encountering intolerable tidal effects.

A second constraint arises from the proper acceleration needed to remain at rest in the wormhole geometry. For static observers, the required acceleration is given by

$$a^\mu = u^\nu \nabla_\nu u^\mu = \left(0, \Phi'(r)\left(1 - \frac{b(r)}{r}\right), 0, 0\right), \tag{78}$$

and must again remain within safe physical bounds. For geodesic travelers, this term vanishes, but practical missions may require hovering or navigation maneuvers that invoke such accelerations.

Figures 12 and 13 illustrate the tidal accelerations experienced by a human-scale traveler in the radial and lateral directions, respectively, as they approach and traverse the wormhole throat. Both plots assume a moderate redshift profile $\Phi(r) = -a/r$ with $a = 0.2$ and a shape function $b(r) = r_0^2/r$, with $r_0 = 1$ representing the throat radius. The shaded region below the dashed line, corresponding to Earth's gravitational acceleration $g_\oplus \approx 9.8\ \mathrm{m/s^2}$, defines the threshold for human-tolerable forces. In both directions, the tidal accelerations peak near the throat and then decrease rapidly as r increases. For $r \gtrsim 1.2$, the radial and lateral accelerations drop below $g_\oplus$, indicating that traversal through

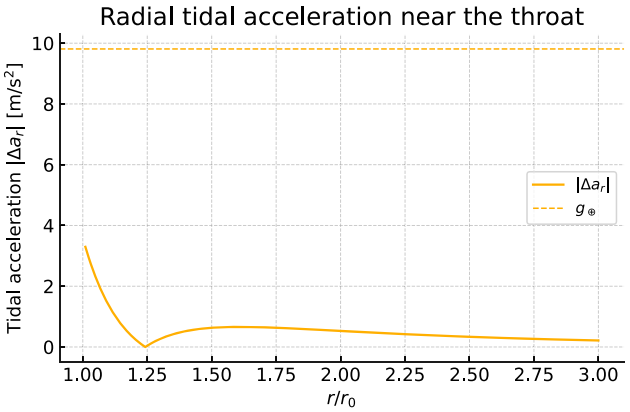

Fig. 12 Radial tidal acceleration $|\Delta a_r|$ for the representative model with $r_0 = 10^8$ m and body size $\xi = 2$ m. The dashed line indicates $g_\oplus$. For $r \gtrsim 1.05\, r_0$, the radial tidal acceleration falls below $g_\oplus$

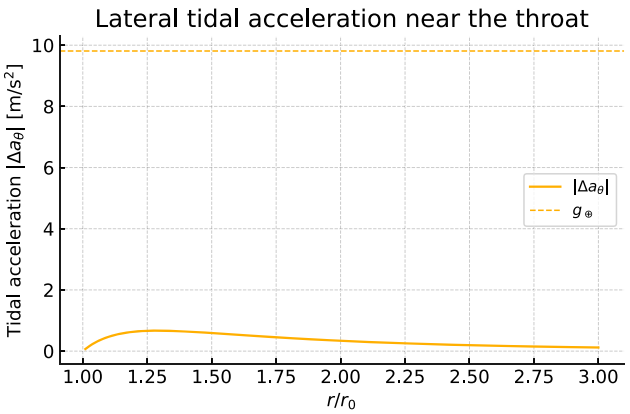

Fig. 13 Lateral tidal acceleration $|\Delta a_\theta|$ for the same model and scales as Fig. 12. The dashed line indicates $g_\oplus$. Lateral tides remain below $g_\oplus$ shortly outside the throat

the wormhole becomes physically tolerable just outside the immediate throat region. The lateral tidal forces are slightly weaker than the radial ones, a common feature in spherically symmetric and mildly rotating spacetimes. These results demonstrate that, with carefully chosen redshift and shape functions, the tidal environment within a rotating wormhole can be rendered navigable for hypothetical travelers. Furthermore, in $f(R)$ gravity, the presence of higher-order curvature corrections smoothens the geometry near the throat, which indirectly helps reduce tidal gradients. This confirms the physical plausibility of the wormhole not just as a mathematical object, but as a potentially traversable configuration consistent with human-scale tolerances.

7.3 Concrete traversability example (comfort margins)

To make the traversability bounds explicit, we evaluate the orthonormal-frame tidal eigenvalues (static/slow-rotation limit),

$$\mathcal{R}_{\hat{r}\hat{r}\hat{r}\hat{r}} \equiv R_{\hat{r}\hat{r}\hat{r}\hat{r}}, \quad \mathcal{R}_{\hat{t}\hat{\theta}\hat{t}\hat{\theta}} \equiv R_{\hat{t}\hat{\theta}\hat{t}\hat{\theta}},$$

for the representative model used throughout ($b(r) = r_0^2/r$, $\Phi(r) = -0.2/r$), evaluated in the equatorial plane. The slow-rotation diagonal sector coincides with the static one to leading order ($\mathcal{O}(\Omega^2)$ corrections are negligible here given $|\Omega r| \lesssim 0.04$).

A fiducial traveler of size $L = 2$ m experiences tidal accelerations

$$a_{\rm rad} \simeq c^2 \left|\mathcal{R}_{\hat{r}\hat{r}\hat{r}\hat{r}}\right| L, \quad a_{\rm lat} \simeq c^2 \left|\mathcal{R}_{\hat{t}\hat{\theta}\hat{t}\hat{\theta}}\right| L,$$

and a characteristic curvature timescale[3] $f_c \sim (2\pi)^{-1} c\sqrt{|\mathcal{R}|}$. We adopt a conservative comfort requirement $a \lesssim 1\, g$ and a frequency cutoff $f_c \lesssim f_{\rm cut} = 1$ Hz. Setting a macroscopic throat scale $r_0 = 10^8$ m, we obtain the illustrative values in Table 8 and the radial profiles in Figs. 14 and 15.

For a macroscopic throat $r_0 = 10^8$ m and a human-scale traveler ($L = 2$ m), both peak tidal accelerations and curvature frequencies remain comfortably below conservative thresholds ($\lesssim 0.23\, g$ and $\lesssim 0.2$ Hz, respectively). The slow-rotation corrections are $\mathcal{O}(\Omega^2)$ and negligible at the level used elsewhere in the paper, so the traversability conclusions are robust for our parameter choices. Therefore, our analysis indicates that traversability is achievable in the rotating wormhole geometries considered here, especially in the presence of $f(R)$ corrections that help regulate curvature gradients. This makes such models not only theoretically stable but also potentially navigable in a physically meaningful sense, further enhancing their viability as candidates for exotic but traversable spacetimes.

8 Results and discussion

Our analysis demonstrates that the inclusion of $f(R)$ corrections, particularly for models of the form $f(R) = R + \alpha R^2$, leads to a significant reduction in the severity of null energy condition (NEC) violations near the wormhole throat. These higher-order curvature terms introduce effective geometric contributions to the stress-energy tensor, which can partially compensate for the exotic matter usually required in such geometries. Specifically, the additional terms arising from the variation of $F(R) = df/dR$ contribute positively to the effective energy–momentum tensor, effectively shifting part of the energy condition burden from the matter sector to the geometric sector.

In the vicinity of the throat, where classical wormhole solutions typically exhibit strong NEC violations, we observe

[3] Equivalently, $f_c = (2\pi)^{-1} c\sqrt{|\mathcal{R}|}$, with $\mathcal{R}$ any of the above curvature eigenvalues in SI units.

Table 8 Tidal-acceleration "comfort" diagnostics for a traveler of size $L = 2$ m and a macroscopic throat $r_0 = 10^8$ m. The largest acceleration near the throat remains $\lesssim 0.23\,g$, and the curvature frequencies are $\lesssim 0.2$ Hz, below a conservative comfort cutoff $f_{\rm cut} = 1$ Hz. Rotation effects are $\mathcal{O}(\Omega^2)$ and below a few percent for the parameters used here

r/r_0	$\mathcal{R}_{\hat{r}\hat{r}\hat{r}\hat{r}}$ [m^{-2}]	$\mathcal{R}_{\hat{t}\hat{\theta}\hat{t}\hat{\theta}}$ [m^{-2}]	$a_{\rm rad}$ [g]	$a_{\rm lat}$ [g]	$f_{\rm rad}$ [Hz]	$f_{\rm lat}$ [Hz]
1.05	1.28×10^{-17}	1.61×10^{-18}	0.234	0.029	0.17	0.060
1.20	1.55×10^{-18}	3.54×10^{-18}	0.028	0.065	0.059	0.090
1.50	3.51×10^{-18}	3.29×10^{-18}	0.064	0.060	0.089	0.087

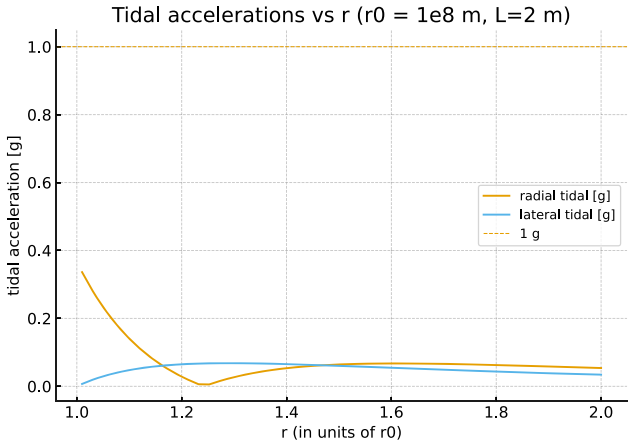

Fig. 14 Radial and lateral tidal accelerations (in units of g) for $r \in [1.01, 2]\,r_0$ with $(r_0, L) = (10^8$ m, 2 m). The dashed line is $1\,g$. The peak $\lesssim 0.23\,g$ occurs near $r \simeq 1.05\,r_0$

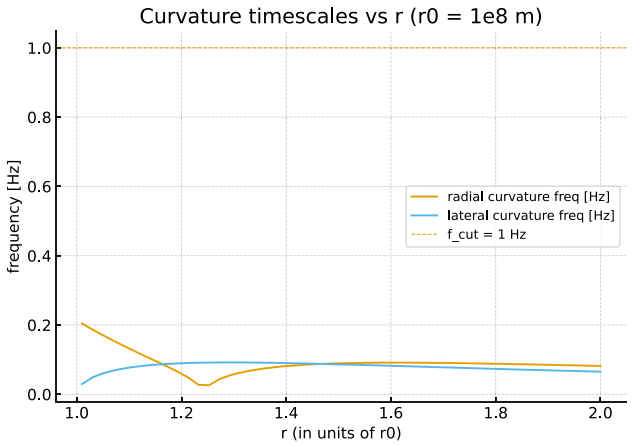

Fig. 15 Curvature timescales cast as frequencies $f_c = (2\pi)^{-1} c\sqrt{|\mathcal{R}|}$ for the same setup. The dashed line marks $f_{\rm cut} = 1$ Hz; all values lie well below

a softening of this requirement due to the $f(R)$-induced geometric terms. This is especially evident in the perturbative regime for small $\alpha > 0$, where the Ricci-squared corrections lead to localized suppression of negative energy densities. While NEC violation is not completely eliminated in most configurations, its magnitude is substantially reduced, particularly for shape functions with mild curvature gradients such as $b(r) = r_0 \log(r + 1)$ or $b(r) = r_0$.

Furthermore, the compatibility of rotating wormhole geometries with $f(R)$ gravity appears to depend sensitively on the angular velocity profile $\Omega(r)$. Among various candidates, profiles with exponential damping, such as $\Omega(r) = \Omega_0\, e^{-\beta r}$, are found to produce a more favorable interplay with the curvature corrections. These profiles not only contribute less severely to the off-diagonal terms in the effective field equations but also help maintain frame-dragging effects within acceptable physical limits. This suggests that rotation can be accommodated in a controlled manner without dramatically increasing the need for exotic matter, provided that the angular velocity decreases sufficiently fast with radius.

Interestingly, for certain combinations of redshift and shape functions, the effective NEC – evaluated using the combined Casimir, thermal, and curvature-induced terms – can be satisfied in a localized region around the throat. This points to the possibility of constructing wormhole solutions that are effectively non-exotic, at least in a restricted radial domain. Although complete satisfaction of all classical energy conditions remains out of reach due to the persistent negative contributions from the Casimir vacuum, the $f(R)$ corrections offer a pathway to partially restore energy condition compliance.

These results reinforce the broader conclusion that modified gravity frameworks such as $f(R)$ gravity not only provide theoretical flexibility for supporting traversable wormholes but also offer practical advantages in reducing the reliance on unphysical matter sources. The mitigation of NEC violations, improved stability characteristics, and enhanced traversability afforded by higher-order curvature terms collectively suggest that rotating wormholes in $f(R)$ gravity occupy a more physically plausible region of the theoretical landscape than their general relativistic counterparts.

9 Conclusions

The present study connects and extends three main research threads: rotating wormholes in general relativity [17], Casimir-type exotic sources [4,18], and wormhole solutions in $f(R)$ gravity [19]. Previous works typically examined only one or two of these elements in isolation. Here we have treated all three in concert, deriving the slow-rotation cor-

rections to the Casimir-supported $f(R)$ geometry, verifying energy conditions, flare-out, and horizon avoidance explicitly, and quantifying traversability via stability and tidal-force criteria. In this sense, our results both test and complement earlier GR and modified-gravity analyses, providing a reference model that can be generalized to other higher-curvature theories or more rapid rotation.

In this work, we have extended the framework of rotating Casimir wormholes to the domain of $f(R)$ gravity, a prominent class of modified gravitational theories that generalize the Einstein–Hilbert action through higher-order curvature terms. By incorporating modifications of the form $f(R) = R+\alpha R^2$, we have demonstrated that geometric contributions from the extended gravitational sector can significantly mitigate the severity of null energy condition (NEC) violations, particularly near the wormhole throat where such violations are typically most pronounced.

Our findings indicate that the inclusion of $f(R)$ corrections gives rise to an effective stress-energy tensor in which part of the exotic matter burden is shifted onto the geometry itself. This effect becomes particularly compelling when combined with judicious choices of wormhole shape and redshift functions, as well as rotational profiles that decay appropriately with radial distance. In such scenarios, NEC violations may be softened or even satisfied in an effective sense, rendering the wormhole configurations more physically viable than their counterparts in standard general relativity. While our representative example shows an interval near the throat where the effective NEC is satisfied, this behavior is localized and parameter-dependent. It should therefore be interpreted as mitigation of NEC violations rather than a generic elimination across the full spacetime domain.

Moreover, we have shown that rotation, while adding complexity to the spacetime structure, can be consistently incorporated within the $f(R)$ framework without destabilizing the solution, provided that the angular velocity profile is appropriately constrained. This interplay between modified gravity, quantum vacuum effects, and rotation opens new avenues for constructing wormhole geometries that are not only mathematically consistent but also potentially stable and traversable under realistic conditions.

Looking ahead, several promising directions for future research remain. Numerical investigations of fully nonperturbative solutions in specific $f(R)$ models could offer deeper insights into the global structure and parameter space of viable wormhole geometries. Stability analyses that go beyond scalar perturbations to include axial and tensorial modes would help assess the robustness of these solutions under more general fluctuations. Additionally, embedding these models within broader scalar-tensor or Horndeski-type theories may reveal new classes of traversable wormholes with richer phenomenology and potential observational signatures.

Therefore, this study supports the growing perspective that modified gravity theories such as $f(R)$ gravity offer a fertile ground for re-examining the viability of exotic spacetimes. By alleviating some of the most prohibitive energy condition constraints, they bring us a step closer to realizing traversable wormholes as solutions that are not only theoretically permissible but potentially compatible with semiclassical and quantum-gravitational expectations.

Funding None.

Data Availability Statement This manuscript has no associated data. [Author's' comment: Data sharing not applicable to this article as no datasets were generated or analysed during the current study.].

Code Availability Statement This manuscript has no associated code/software. [Author's comment: Code/Software sharing not applicable to this article as no code/software was generated or analysed during the current study.].

Funded by SCOAP[3].

Appendix A: Geometric ingredients and field equations for the rotating ansatz

We work consistently with

$$f(R) = R + \alpha R^2, \quad F(R) \equiv \frac{df}{dR} = 1 + 2\alpha R,$$

in the joint small-α and slow-rotation regime, $|\alpha R| \ll 1$ and $|\Omega r| \ll 1$ (cross terms $\mathcal{O}(\alpha\,\Omega^2)$ neglected). Our metric ansatz is (see Eq. (4)),

$$ds^2 = -e^{2\Phi(r)}dt^2 + \frac{dr^2}{1-b(r)/r} + r^2 \times \left[d\theta^2 + \sin^2\theta\,(d\phi - \Omega(r)\,dt)^2\right]. \tag{79}$$

It is convenient to denote

$$A(r) \equiv e^{2\Phi(r)}, \quad B(r) \equiv 1 - \frac{b(r)}{r}.$$

A.1 Christoffel symbols needed at $\mathcal{O}(\Omega)$

To first order in Ω (i.e. keeping $g_{t\phi} = -r^2 \sin^2\theta\, \Omega$ but dropping Ω^2 in g_{tt}, $g_{\phi\phi}$), the nonzero symbols used below are

$$\Gamma^r{}_{tt} = \tfrac{1}{2} g^{rr}\partial_r g_{tt} = B\,A\,\Phi', \quad \Gamma^r{}_{rr} = -\frac{B'}{2B}, \quad \Gamma^r{}_{\theta\theta} = -rB,$$
$$\Gamma^r{}_{\phi\phi} = -rB\,\sin^2\theta,$$
$$\Gamma^r{}_{t\phi} = -\tfrac{1}{2} g^{rr}\partial_r g_{t\phi} = B\,\sin^2\theta\Big(r\,\Omega + \tfrac{1}{2} r^2\Omega'\Big), \tag{80}$$

and the usual spherical ones (e.g. $\Gamma^\theta{}_{\phi\phi} = -\sin\theta\cos\theta$). Primes denote d/dr.

A.2 Ricci tensor/scalar to the required order

Decomposing into a static part and a rotational correction,

$$R_{\mu\nu} = R^{(0)}_{\mu\nu} + \delta R_{\mu\nu}, \quad R = R^{(0)} + \mathcal{O}(\Omega^2),$$

the diagonal components $R^{(0)}_{\mu\nu}$ are those of the static Morris–Thorne metric with $A = e^{2\Phi}$ and $B = 1 - b/r$, while the off-diagonal correction is $\delta R_{t\phi} = \mathcal{O}(\Omega, \Omega')$. It is convenient to quote the corresponding Einstein tensor components for the static sector (they will enter Eq. (87) below):

$$G^t{}_t = \frac{b'}{r^2}, \quad G^r{}_r = -\frac{b}{r^3} + \frac{2B\,\Phi'}{r},$$
$$G^\theta{}_\theta = G^\phi{}_\phi = B\Big(\Phi'' + \Phi'^2 + \frac{\Phi'}{r}\Big) - \frac{(b'r - b)}{2r^2}\Big(\Phi' + \frac{1}{r}\Big), \tag{81}$$

so that

$$R^{(0)}(r) = -\Big(G^t{}_t + G^r{}_r + 2G^\theta{}_\theta\Big), \tag{82}$$

and $R = R^{(0)} + \mathcal{O}(\Omega^2)$ in the slow-rotation limit.

The rotational piece needed below can be written compactly as

$$R_{t\phi} = -\frac{1}{2} r^2 \sin^2\theta\; \mathcal{L}[\Omega] + \mathcal{O}(\Omega^3), \tag{83}$$

where the radial differential operator acting on Ω is

$$\mathcal{L}[\Omega] = B\,\Omega'' + \Big(\frac{4B}{r} + B' - 2B\,\Phi'\Big)\Omega' + \Big(\frac{2B'}{r} - \frac{2B\,\Phi'}{r}\Big)\Omega. \tag{84}$$

A.3 Covariant derivatives of $F(R)$ for $F = F(r)$

Since $R = R(r) + \mathcal{O}(\Omega^2)$, we have $F(R) = F(r)$ and

$$\nabla_r\nabla_r F = F'' - \Gamma^r{}_{rr} F' = F'' + \frac{B'}{2B} F',$$
$$\nabla_t\nabla_t F = -\Gamma^r{}_{tt} F' = -B\,A\,\Phi'\,F',$$
$$\nabla_\theta\nabla_\theta F = -\Gamma^r{}_{\theta\theta} F' = rB\,F',$$
$$\nabla_\phi\nabla_\phi F = -\Gamma^r{}_{\phi\phi} F' = rB\,\sin^2\theta\,F',$$
$$\nabla_t\nabla_\phi F = -\Gamma^r{}_{t\phi} F' = -B\,\sin^2\theta\Big(r\,\Omega + \tfrac{1}{2} r^2\Omega'\Big)\,F'. \tag{85}$$

The d'Alembertian $\Box F \equiv g^{\mu\nu}\nabla_\mu\nabla_\nu F$ then reduces to

$$\Box F = B\,F'' + \Big(B\,\Phi' + \tfrac{1}{2} B' + \frac{2B}{r}\Big)F' + \mathcal{O}(\Omega^2). \tag{86}$$

A.4 Modified field equations in component form

The $f(R)$ equations can be cast in the compact form

$$F\,G_{\mu\nu} + \frac{1}{2}(f - RF)g_{\mu\nu} + \Big(\nabla_\mu\nabla_\nu - g_{\mu\nu}\Box\Big)F = \kappa\,T_{\mu\nu}. \tag{87}$$

For $f = R + \alpha R^2$ one has $f - RF = -\alpha R^2$. Keeping terms up to $\mathcal{O}(\Omega)$, the *diagonal* equations use the static $G_{\mu\nu}$ from (81) and the derivative operators (85)-(86):

$$\begin{aligned}
\textbf{tt:}\quad & F\,G_{tt} - \tfrac{1}{2}\alpha R^2 g_{tt} + \nabla_t\nabla_t F - g_{tt}\Box F = \kappa\,T_{tt},\\
\textbf{rr:}\quad & F\,G_{rr} - \tfrac{1}{2}\alpha R^2 g_{rr} + \nabla_r\nabla_r F - g_{rr}\Box F = \kappa\,T_{rr},\\
\theta\theta:\quad & F\,G_{\theta\theta} - \tfrac{1}{2}\alpha R^2 g_{\theta\theta} + \nabla_\theta\nabla_\theta F - g_{\theta\theta}\Box F = \kappa\,T_{\theta\theta},\\
\phi\phi:\quad & F\,G_{\phi\phi} - \tfrac{1}{2}\alpha R^2 g_{\phi\phi} + \nabla_\phi\nabla_\phi F - g_{\phi\phi}\Box F = \kappa\,T_{\phi\phi}.
\end{aligned} \tag{88}$$

To first order in rotation, the *off-diagonal* $t\phi$ equation is particularly informative. Since $g_{t\phi} = \mathcal{O}(\Omega)$, the terms proportional to $g_{t\phi}$ in (87) enter at higher order and can be dropped. Using (83) and (85),

$$F\,R_{t\phi} + \nabla_t\nabla_\phi F = \kappa\,T_{t\phi} \Longrightarrow -\frac{1}{2} r^2\sin^2\theta\,F\,\mathcal{L}[\Omega] - B\,\sin^2\theta\Big(r\,\Omega + \tfrac{1}{2} r^2\Omega'\Big)\,F' = \kappa\,T_{t\phi}. \tag{89}$$

Dividing by $\sin^2\theta$ yields a second-order radial ODE for $\Omega(r)$:

$$F\,\mathcal{L}[\Omega] + \frac{2B}{r^2}\Big(r\,\Omega + \tfrac{1}{2} r^2\Omega'\Big)\,F' = -\frac{2\kappa}{r^2}\,T_{t\phi}, \tag{90}$$

with $\mathcal{L}[\Omega]$ given in (84). In GR ($\alpha = 0 \Rightarrow F \equiv 1$) and for a perfect fluid with vanishing $T_{t\phi}$, Eq. (90) reduces to the familiar Hartle slow-rotation equation. Equations above hold for any specified matter sector $T_{\mu\nu}$; in the main text we supply the Casimir-motivated anisotropic fluid (with optional thermal corrections). Boundary conditions for $\Omega(r)$ are regularity at the throat and asymptotic decay (or matching) at large r. All diagonal sectors acquire the $f(R)$ corrections through F and the differential operators acting on $F(r)$, while rotation first enters at $\mathcal{O}(\Omega)$ only through (89).

Appendix B: Conservation of the anisotropic (Casimir) fluid

In the text we model the Casimir-inspired matter as an anisotropic fluid with

$$T_{\mu\nu} = (\rho + \tau_\rho)u_\mu u_\nu + (p_r + \tau_r)n_\mu n_\nu + (p_t + \tau_t)\sigma_{\mu\nu}, \quad (91)$$

and parametrize the matter components as

$$\rho(r) = -\frac{C}{\ell(r)^4}, \quad p_r(r) = w_r\,\rho(r), \quad p_t(r) = w_t\,\rho(r), \quad (92)$$

with effective proper separation

$$\ell(r) = \ell_0 \left(\frac{r}{r_0}\right)^\gamma. \quad (93)$$

Below we verify $\nabla_\mu T^{\mu\nu} = 0$ in the slow-rotation regime (neglecting terms of order Ω^2). For static, spherically symmetric/diagonal metric sectors the radial component of the conservation law gives the standard anisotropic-fluid identity,

$$\frac{dp_r}{dr} = -(\rho + p_r)\,\Phi'(r) - \frac{2}{r}\,(p_r - p_t). \quad (94)$$

Substituting the parametrization (92) and using $\rho'(r) = -4\gamma\,\rho(r)/r$ (from $\rho \propto \ell^{-4}$ and $\ell \propto r^\gamma$) yields

$$w_r\left(-\frac{4\gamma}{r}\rho\right) = -(1 + w_r)\rho\,\Phi'(r) - \frac{2}{r}(w_r - w_t)\rho. \quad (95)$$

Canceling the common factor $\rho(r)$ (nonzero except at spatial infinity) and multiplying by r gives the closure relation

$$4\gamma\, w_r = (1 + w_r)\, r\Phi'(r) + 2(w_r - w_t). \quad (96)$$

Equation (96) is a necessary and sufficient condition for the radial conservation equation to hold exactly in the static/slow-rotation approximation used in this work. It simply relates the power-law exponent γ of the local plate separation to the anisotropy parameters w_r, w_t and the redshift gradient $r\Phi'(r)$. Thus $\ell(r)$ is not arbitrary: choosing $\ell(r)$ with the exponent γ fixed by (96) ensures $\nabla_\mu T^{\mu\nu} = 0$ for matter that depends only on r.

With the representative choices used repeatedly in the main text,

$$w_r = -3, \quad w_t = +1, \quad \Phi(r) = -\frac{0.2}{r} \Rightarrow r\Phi'(r) = 0.2,$$

Equation (96) gives

$$4\gamma(-3) = (1 - 3)\cdot 0.2 + 2(-3 - 1) = -0.4 - 8 = -8.4,$$

hence

$$\gamma = \frac{-8.4}{-12} = 0.70.$$

Therefore the choice

$$\ell(r) = \ell_0 \left(\frac{r}{r_0}\right)^{0.70}$$

ensures $\nabla_\mu T^{\mu\nu} = 0$ identically (within the slow-rotation approximation) for the anisotropic Casimir fluid used in our numerical examples. A symbolic one-line check of the radial conservation reduced to Eq. (96) is provided in the main text for clarity (If thermal corrections τ_i are retained, the same algebra applies provided their radial dependence is included in $\rho(r)$ and the above derivative; for the baseline plots we set $\tau_i = 0$.).

References

1. M.S. Morris, K.S. Thorne, Am. J. Phys. **56**, 395 (1988)
2. F.S.N. Lobo, *Classical and Quantum Gravity Research* (Nova Science, New York, 2008). arXiv:0710.4474 [gr-qc]
3. M. Visser, *Lorentzian Wormholes: From Einstein to Hawking* (AIP, Washington, 1995)
4. R. Garattini, Eur. Phys. J. C **79**, 951 (2019)
5. S.A. Fulling, L. Parker, B.L. Hu, Phys. Rev. D **10**, 3905 (1974)
6. D. Deutsch, P. Candelas, Phys. Rev. D **20**, 3063 (1979)
7. K.A. Milton, *The Casimir Effect: Physical Manifestations of Zero-Point Energy* (World Scientific, Singapore, 2001)
8. L.H. Ford, T.A. Roman, Phys. Rev. D **53**, 5496 (1996)
9. R. Garattini, A.G. Tzikas, Eur. Phys. J. C **85**(3), 336 (2025)
10. T.P. Sotiriou, V. Faraoni, Rev. Mod. Phys. **82**, 451 (2010)
11. A. Felice, S. Tsujikawa, Living Rev. Relativ. **13**, 3 (2010)
12. S. Nojiri, S.D. Odintsov, Int. J. Geom. Methods Mod. Phys. **4**, 115 (2007)
13. G.J. Olmo, D. Rubiera-Garcia, Class. Quantum Gravity **37**(21), 215002 (2020)
14. S. Capozziello, M. Laurentis, Phys. Rep. **509**, 167 (2011)
15. F.F. Santos, J. Hologr. Appl. Phys. **4**(3), 1–10 (2024)
16. F. Baziar, J. Hologr. Appl. Phys. **5**, 3 (2025). https://doi.org/10.22128/jhap.2025.1041.1122
17. E. Teo, Phys. Rev. D **58**, 024014 (1998)
18. P.K.F. Kuhfittig, J. High Energy Phys. Gravit. Cosmol. **9**, 295–300 (2023)
19. F.S.N. Lobo, M.A. Oliveira, Phys. Rev. D **80**, 104012 (2009)
20. K. Jusufi, A. Övgün, Phys. Rev. D **97**, 024042 (2018)
21. W. Javed, R. Babar, A. Övgün, Phys. Rev. D **99**, 084012 (2019)
22. A. Övgün, G. Gyulchev, K. Jusufi, Ann. Phys. **406**, 152–172 (2019)
23. W. Javed, S. Riaz, R.C. Pantig, A. Övgün, Eur. Phys. J. C **82**, 1057 (2022)
24. P. Panyasiripan, N. Kaewkhao, P. Channuie, A. Övgün, Nucl. Phys. B **1004**, 116563 (2024)
25. A.A. Araújo Filho, J.A.A.S. Reis, A. Övgün, Eur. Phys. J. C **85**, 83 (2025)
26. P. Channuie, A. Ditta, N. Kaewkhao, A. Övgün, Phys. Dark Universe **48**, 101963 (2025)
27. B. Bhawal, S. Kar, Phys. Rev. D **46**, 2464 (1992)
28. A.A. Starobinsky, Phys. Lett. B **91**, 99 (1980)
29. A. De Felice, S. Tsujikawa, Living Rev. Relativ. **13**, 3 (2010)
30. T. Clifton, P.G. Ferreira, A. Padilla, C. Skordis, Phys. Rep. **513**, 1 (2012)
31. M. Visser, Phys. Rev. D **54**, 5103 (1996)
32. T. Kobayashi, T. Tanaka, Phys. Rev. D **71**, 084005 (2005)